

Simultaneous Multi-Wavelength Observations of Sgr A* during 2007 April 1-11

F. Yusef-Zadeh¹, H. Bushouse², M. Wardle³, C. Heinke⁴, D. A. Roberts⁵, C.D. Dowell⁶, A. Brunthaler⁷, M. J. Reid⁸, C. L. Martin⁹, D. P. Marrone¹⁰, D. Porquet¹¹, N. Grosso¹¹, K. Dodds-Eden¹², G. C. Bower¹³, H. Wiesemeyer¹⁴, A. Miyazaki¹⁵, S. Pal¹⁶, S. Gillessen¹², A. Goldwurm¹⁷, G. Trap¹⁸, and H. Maness¹³

ABSTRACT

We report the detection of variable emission from Sgr A* in almost all wavelength bands (i.e. centimeter, millimeter, submillimeter, near-IR and X-rays) during a multi-wavelength observing campaign. Three new moderate flares are detected simultaneously in both near-IR and X-ray bands. The ratio of X-ray to near-IR flux in the flares is consistent with inverse Compton scattering of near-IR photons by submillimeter emitting relativistic particles which follow scaling relations obtained from size measurements of Sgr A*. We also find that the flare statistics in near-IR wavelengths is consistent with the probability of flare emission being inversely proportional to the flux. At millimeter wavelengths, the presence of flare emission at 43 GHz (7mm) using VLBA with milli-arcsecond spatial resolution indicates the first direct evidence that hourly time scale flares are localized within the inner 30×70 Schwarzschild radii of Sgr A*. We also show several cross correlation plots between near-IR, millimeter and submillimeter light curves that collectively demonstrate the presence of time delays between the peaks of emission up to three hours. The evidence for time delays at millimeter and submillimeter wavelengths are consistent with the source of emission being optically thick initially followed by a transition to an optically thin regime. In particular, there is an intriguing correlation between the optically thin near-IR and X-ray flare and optically thick radio flare at 43 GHz that occurred on 2007 April 4. This would be the first evidence of a radio flare emission at 43 GHz delayed with respect to the near-IR and X-ray flare emission. The time delay measurements support the expansion of hot self-absorbed synchrotron plasma blob and weaken the hot spot model of flare emission. In addition, a simultaneous fit to 43 and 84 GHz light curves, using an adiabatic expansion model of hot plasma, appears to support a power law rather than a relativistic Maxwellian distribution of particles.

Subject headings: accretion, accretion disks — black hole physics — Galaxy: center

1. Introduction

The black hole at the center of our own galaxy was first detected as the radio source Sgr A* over 30 years ago (Balick & Brown 1974). It was found to lie at the center of a cluster of young massive stars. Submillimeter and far-infrared observations showed that Sgr A* is encircled by a torus of gas approximately 10 light-years across, which orbits with a speed of 100 km s^{-1} (e.g. Genzel & Townes 1987). The gravity required to hold onto this material implies a mass of several million solar masses, although a portion of this is contributed by the stars in the stellar cluster. These measurements suggested that Sgr A* could be a black hole. More detail was provided through studies of the light distribution of stars in the cluster, as well as the motions of ionized and molecular gas clouds orbiting Sgr A*. These measurements implied a mass of approximately 3–4 million times that of the sun (Genzel 2000; Genzel & Townes 1987) lying within a third of a light year of the radio source. Recently, more precise measurements of fast moving stars in close orbits around Sgr A* have conclusively demonstrated that it has a mass of $\sim 4 \times 10^6 M_{\odot}$ (Ghez et al. 2005; Eisenhauer et al. 2005; Ghez et al. 2008; Schödel et al. 2002; Gillessen et al. 2009) and that the size of the radio source is about ~ 4 times its Schwarzschild radius at 230 GHz (R_s) (Doeleman et al. 2008). This dark, massive object has also been uniquely identified through the proper motion of the radio source, which show that Sgr A* must contain $> 4 \times 10^5 M_{\odot}$ (Reid & Brunthaler 2004). Taken together, these measurements provide strong evidence that Sgr A* is a black hole with mass $\sim 4 \times 10^6 M_{\odot}$. No other known category of astrophysical object can easily fit so much mass into a sub-AU-size region.

¹Dept. of Physics and Astronomy, Northwestern University, Evanston, IL 60208

²STScI, 3700 San Martin Drive, Baltimore, MD 21218

³Department of Physics and Engineering, Macquarie University, Sydney NSW 2109, Australia

⁴Dept. of Physics, University of Alberta, Room #238 CEB, 11322-89 Avenue, Edmonton AB T6G 2G7, Canada

⁵Adler Planetarium and Astronomy Museum, 1300 South Lake Shore Drive, Chicago, IL 60605

⁶Cal Tech, Jet Propulsion Laboratory, Pasadena, CA 91109

⁷Max-Planck-Institut für Radioastronomie, Auf dem Huegel 69, 53121 Bonn, Germany

⁸Harvard-Smithsonian CfA, 60 Garden Street, Cambridge, MA 02138

⁹Oberlin College, Dept. of Physics and Astronomy, Professor 110 N. St., Oberlin, OH 44074

¹⁰National Radio Astronomy Observatory; University of Chicago, 5640 South Ellis Avenue, Chicago IL 60637

¹¹Observatoire astronomique de Strasbourg, Université de Strasbourg, NRS, INSU, 11 rue de l'Université, 67000 Strasbourg, France

¹²Max-Planck-Institut für Extraterrestrische Physik 1312, D-85471, Garching, Germany

¹³Radio Astronomy Lab, 601 Campbell Hall, University of California, Berkeley, CA 94720

¹⁴Institut de RadioAstronomie Millimétrique, 300 rue de la Piscine, Domaine Universitaire 38406 Saint Martin d'Heres, France, on leave to IRAM Granada, Spain

¹⁵Mizusawa VLBI Observatory, National Astronomical Observatory of Japan, Mizusawa, Oshu, Iwate 023-0861, Japan

¹⁶School of Physics, University of Western Australia, 35 Stirling Highway, Crawley, WA, 6009, Australia

¹⁷Service d'Astrophysique / IRFU / DSM, CEA Saclay, Bat. 709, 91191, Gif-sur-Yvette Cedex, France and AstroParticule & Cosmologie (APC) / Université Paris VII / CNRS / CEA / Observatoire de Paris Bat. Condorcet, 10, rue Alice Domon et Léonie Duquet, 75205 Paris Cedex 13, France

This massive black hole is a hundred times closer to us than the next nearest example, presenting an unparalleled opportunity to closely study the process by which gas is captured by black holes. It is therefore the subject of intense scrutiny. The energy radiated by Sgr A* is thought to be liberated from gas that is falling into the black hole after being captured from the powerful winds of members of its neighboring cluster of massive stars (e.g., Melia 1992). The broad band spectrum of Sgr A* peaks at submillimeter wavelengths (Zylka et al. 1992; Falcke et al. 1998); this is thought to be the dividing line between optically thick and optically thin emission at low and high frequencies, respectively. The bolometric luminosity of Sgr A* $\sim 100 L_{\odot}$ is several orders of magnitudes below that predicted given its expected rate of capture of material from stellar winds, prompting a number of theoretical models to explain its very low efficiency (Narayan et al. 1995; Liu & Melia 2001; Yuan et al. 2003; Goldston et al. 2005; Liu et al. 2004; Falcke et al. 2009).

Now that the quiescent spectrum of emission from Sgr A* has been characterized from radio to X-rays, attention has turned to variability of emission in multiple wavelengths. These measurements probe the structure and the physical parameters of the hot plasma in the vicinity of the black hole by measuring the time variations of its flux in different wavelength bands as well as their cross-correlation with each other. Flaring activity on $< 1 - 4$ hour time scale is seen in all wavelength bands in which quiescent emission has been detected.

Flaring X-ray emission from Sgr A* has been detected and has been argued to originate within a few Schwarzschild radii of the $\sim 4 \times 10^6 M_{\odot}$ black hole (Baganoff et al. 2003; Goldwurm et al. 2003; Porquet et al. 2003; Bélanger et al. 2005). At near-IR (NIR) wavelengths (Genzel et al. 2003; Yuan et al. 2003; Ghez et al. 2004; Hornstein et al. 2007), flare emission from Sgr A* is shown to be due to optically thin synchrotron emission, whereas the long-wavelength flaring activity in submillimeter, millimeter and centimeter bands is due to optically thick synchrotron emission. The exact frequency at which the transition from optically thick to thin flare emission occurs is unknown.

A variety of mechanisms have been proposed to explain the origin of the variability of Sgr A*. Many of these models have considered different energy distributions for the relativistic particles to explain the origin of submillimeter emission (Markoff et al. 2001; Yuan et al. 2002; Melia 2002; Liu & Melia 2002; Yuan et al. 2003; Nayakshin & Sunyaev 2003; Eckart et al. 2004, 2006a,b; Yusef-Zadeh et al. 2006a; Gillessen et al. 2006; Goldston et al. 2005; Liu et al. 2006; Falcke et al. 2009); Melia and Falcke (2001 and references therein). The direction that has been taken in the past in interpreting the flaring activity of Sgr A* is within one of the established paradigms for the accretion flow that have been developed based on the time-averaged emission – for example a thin accretion disk, a disk and jet, outflow, an advection-dominated accretion flow, radiatively inefficient accretion flow, accretion disk inflow/outflow solutions (Melia 1992; Yuan et al. 2003; Falcke & Markoff 2000; Falcke et al. 2009; Narayan et al. 1998; Blandford & Begelman 1999) and then the predicted spectrum is compared with the observed spectrum.

We have recently analyzed the NIR flaring of Sgr A*, which is produced by synchrotron emission from a transient population of particles produced within ~ 10 Schwarzschild radii of the massive black hole (Genzel et al. 2003; Eckart et al. 2006a; Gillessen et al. 2006). We argued that the $\sim 2 - 3$ hour duration of submillimeter flares could not be due to synchrotron cooling when observed simultaneously with a NIR flare (estimated to be ~ 20 minutes and ~ 12 hours at $1.6\mu\text{m}$ [188 THz] and $850\mu\text{m}$ [350 GHz], respectively). The decline in submillimeter light curves was interpreted to be due to adiabatic cooling associated with expansion of the emitting plasma (Yusef-Zadeh et al. 2006a,b) under the assumption that the same accelerated population of particles is responsible

for NIR and submillimeter emission. Time delays detected between peaks of flare emission at radio, submillimeter and NIR/X-rays wavelengths are consistent with this picture (e.g., Yusef-Zadeh et al. 2006b; Marrone et al. 2008; Yusef-Zadeh et al. 2008; Meyer et al. 2008; Eckart et al. 2008). However, the lack of long simultaneous coverage have not placed strong constraints in time delay measurements, especially between radio and NIR wavelengths. Simple modeling of the total and polarized intensity of the hot expanding plasma provide predictions that can be tested observationally by carrying out observational campaigns such as the one we coordinated during April 2007 to examine the mechanisms for the variability, with implications on the nature of the accretion flow. The results presented here are the third in a series of papers that came from the multi-wavelength observing campaign that took place on 2009 April (Porquet et al. 2008; Dodds-Eden et al. 2009). The results of soft γ -ray observations are given separately (Trap et al. 2009).

The structure of this paper is as follows. §3 presents light curves of all the useful data that were taken in this campaign, following the observational details described in §2. In §4 we analyze the statistical properties of flare emission and the corresponding spectral and power spectrum distributions at NIR wavelengths, as well as cross-correlation analysis of light curves. We then discuss in §5 the origin of X-ray emitting flares and provide observational support for the expanding hot plasma model of flare emission. The polarization results will be given elsewhere.

2. Observations and Data Reduction

The primary purpose of observations made during 2007 April 1-11 was the coordination of several telescopes operating at many wavelengths to monitor the emission from Sgr A* and measure the time evolution of its spectrum. There were a total of 13 observatories that participated in this campaign, including XMM-Newton, the Hubble Space Telescope (HST), the International Gamma-Ray Astrophysics Laboratory INTEGRAL, the Very Large Array (VLA) of the National Radio Astronomy Observatory¹⁸ (NRAO), the Very Long Baseline Array (VLBA¹⁸), the Caltech Submillimeter Observatory (CSO), the Very Large Telescope (VLT), the Submillimeter Array (Blundell 2004), the 30m Pico Veleta Telescope of the Institute for Millimeter Radioastronomy (IRAM), the Submillimeter Telescope (SMT), the Nobeyama Millimeter Array (NMA), the Combined Array for Research in Millimeter-wave Astronomy (CARMA), and the Giant Meterwave Radio Telescope (GMRT). The campaign was organized by first obtaining observing time with XMM-Newton (PI: D. Porquet) and HST (PI: F. Yusef-Zadeh), and then coordinating the ground-based facilities to the allotted space-based schedules.

Figure 1 shows the schedule of all observations and their rough durations. Details of XMM-Newton and VLT/NACO observations have already been reported in Porquet et al. (2008), and (Dodds-Eden et al. 2009), respectively. Summary of the results from VLT/VISIR and INTEGRAL observations has also been given by Trap et al. (2009). Briefly, XMM observations were carried out using three observations for a total of 230 ks blocks of time during 2007 March 30 to April 4, and the VLT/NACO observations took place between 2007 April 1–6 using H (1.66 μm), K (2.12 μm), and L' (3.8 μm) bands. INTEGRAL observations took place in parallel to XMM-Newton on April 1 and 4 for a total effective exposure time of 212 ks for IBIS/ISGRI (20–100 keV) and 46 ks for

¹⁸The National Radio Astronomy Observatory is a facility of the National Science Foundation, operated under a cooperative agreement by Associated Universities, Inc.

JEM-X 1 (3–20 keV).

2.1. HST NICMOS: 1.45 μ m and 1.70 μ m

We obtained 40 orbits of HST observations using the NICMOS camera 1, with the orbits distributed over seven consecutive days between 2007 April 1–7. The observations used the NICMOS F145M and F170M filters, with exposure times of 144 sec in each filter and readout samplings of ~ 16 sec within each exposure. Use of this pair of filters has several advantages. First, they have no overlap in wavelength space and are therefore suitable for spectral index measurements. Second, they are well matched to one another in terms of throughput, so that we can use identical exposure and readout times, thus producing time series data that are evenly sampled in both filters. This has great advantages for making periodicity measurements. Third, their relatively high throughput also allows us to use relatively short exposure times, so that we can cycle back and forth between the two filters fairly rapidly. The near-simultaneous observations then allow us to make meaningful spectral index measurements of flare events. This is especially true for the peaks of flare events, where the flux from Sgr A* does not change rapidly over the course of several minutes or more. The spectral index distribution can not be measured accurately, however, during the rise and fall of flare events because the overall flux is changing more rapidly than the cadence of our filter cycling times.

The IRAF “apphot” routines were used to perform aperture photometry of sources in the NICMOS Sgr A* field, including Sgr A* itself. For stellar sources the measurement aperture was positioned on each source using an automatic centroiding routine. This approach could not be used for measuring Sgr A* because its signal is spatially overlapped by that of the orbiting star S0-2 and S17. Therefore the photometry aperture for Sgr A* was positioned by using a constant offset from the measured location of S0-2 in each image. The offset between S0-2 and Sgr A* was derived from the orbital parameters given by Ghez et al. (2003). The position of Sgr A* was estimated to be 0.16'' south and 0.01'' west of S0-2 at the time of the HST observations. To confirm the accuracy of the position of Sgr A*, two images of Sgr A* taken before and during a flare event were aligned and subtracted, which resulted in an image showing the location of the flare emission.

We used a measurement aperture with a diameter of 3 detector pixels, which corresponds to $\sim 0.13''$. This size was chosen as a suitable compromise between wanting to maximize the fraction of the Sgr A* PSF included in the aperture, while at the same time limiting the amount of signal coming from the wings of the PSF from the adjacent star S0-2. We derived aperture correction factors by making measurements of a reasonably well isolated star in the field through a series of apertures of increasing size. The aperture corrections, which convert the fluxes measured through our 3-pixel diameter aperture to a semi-infinite aperture, are 2.91 and 3.40 for the 1.45 and 1.70 μ m bands, respectively. Absolute calibration of the photometric measurements was accomplished using the latest calibrations for the NICMOS F145M and F170M obtained from STScI.

De-reddened fluxes were computed using the appropriate extinction law for the Galactic center (Moneti et al. 2001) and their extinction value of $A(K)=3.3$ mag. These translate to extinction values for the NICMOS filter bands of $A(F170M)=5.03$ mag and $A(F145M)=6.52$ mag, which then correspond to correction factors of 103 and 406, respectively. Because there is some contribution from the neighboring star S0-2 within our measurement aperture, we have determined the flux of Sgr A* when it is flaring by subtracting the mean flux level measured during “quiescent” episodes. The resulting net flux can therefore be safely attributed to Sgr A* flares.

2.2. VLA: 43 and 22 GHz

We used a fast-switching technique to observe Sgr A* simultaneously using the VLA D configuration at 43.3 GHz (7mm) and 22.4 GHz (13mm) GHz. These observations took place on 2007 April 1–4, each lasting for ~ 7 hours, using 8 VLA and 18 eVLA antennas. The two IFs were separated by 50MHz in each observation, except for those on 2007 April 4, when the two IFs were centered at non-standard frequencies of 43.1851 and 43.5351 GHz, which corresponds to a frequency separation of 350 MHz. The separation was used to carry out polarization measurements, the result of which will be given elsewhere.

We cycled between Sgr A* and the fast-switching calibrator 17444-31166 (2.3 degrees away from Sgr A*) for 90 sec and 30 sec, respectively, throughout the observation. On 2007 April 4, we also used the fast-switching phase calibrator 17459-28204, which is weaker, but closer ($\sim 21'$) to Sgr A*. 3C286 was used as the flux calibrator and NRAO530 was observed as a polarization and additional phase calibrator. The light curves at 43 GHz restricted data to a uv range greater than 90 k λ with full width at half point of $2.45'' \times 1.3''$ (PA= -4^0). We used NRAO530 for pointing every 30 minutes; the bootstrapped flux of NRAO530 at 43 GHz is 2.43 ± 0.05 Jy. At 22 GHz, the strong continuum emission from ionized gas associated with extended features surrounding Sgr A* overwhelmed the flux of Sgr A* itself, making the variability analysis uncertain. Therefore the 22 GHz data are not useful and are not presented here. In all the measurements presented here, we used only antennas that had constant gain curves with similar values, thus many of the eVLA antennas were not used.

In all cases, at least two and sometimes three phase calibrators were used in order to ensure that amplitude variability or calibration errors of one of the calibrators would not be introduced into the light curve of Sgr A*. In the case of multiple phase calibrators, the same calibrator used to calibrate the gains of Sgr A* was used to cross-calibrate the other calibrators. In cases where calibrator light curves are shown as alongside those of Sgr A*, they were obtained from cross-calibration using one of the other phase calibrators and *not* from self-calibration. Additionally, as a check, all light curves of Sgr A* made using phase calibrations from the principle phase calibrator (usually 17444-31166) were compared against light curves of Sgr A* made using the other phase calibrators. These comparisons were used to identify bad data in the calibrators and after editing and recalibration light curves using different calibrators were consistent.

For the final light curves of Sgr A*, the data were calibrated using the principle phase calibrator (17444-31166). A phase self-calibration was applied to Sgr A* before the determination of a light curve. No amplitude self-calibration was done to Sgr A* or any backup phase calibrators, whose light curves are shown as a reference, since amplitude calibration would remove time variation from the light curves. After phase self-calibration, large images were made and found no confusing point sources above the rms noise (typically 2.5 mJy beam $^{-1}$ in a full run at 43 GHz) when the selected uv data were greater than 90k λ .

In order to derive the light curve in the visibility plane, the Astronomical Image Processing System (AIPS) task DFTPL was used. DFTPL plots the direct Fourier transform of a vector averaged set of measured visibilities as a function of time. Since we use this on data that has been phase self-calibrated using the point source Sgr A*, the vector average gives the flux of Sgr A*. Visibilities are averaged in bins with defined time widths, however, since the number of visibilities in each bin varies, the error associated with the average will not be constant and are derived at each time range.

2.3. VLBA: 43, 22, and 15 GHz

We observed Sgr A* with the VLBA in two different experiments. One took place on 2007 April 1, 5 and 11 at 43 GHz under program BR124. All observations employed four 8 MHz bands in dual circular polarization each. These observations were made at 43 GHz and involved rapid switching between Sgr A* and the two background continuum sources J1748-291 and J1745-283. Sources were changed every 15 seconds in the sequence Sgr A* – J1748-291 – Sgr A* – J1745-283 – Sgr A*, yielding an on-source time of ~ 10 seconds. Before, in the middle, and after each observation 16 quasars were observed within ~ 40 minutes. NRAO 530 was also observed as fringe-finder. The total observing time including the quasars was 8 hours for each observation. The data were correlated with 16 spectral channels per frequency band and an integration time of 0.131 seconds. The ~ 1 hour gaps in the light curves of Sgr A* are due to geodetic measurements.

In the second experiment (proposal code BB230), the observations on 2007 April 2 and 10 involved rapid switching between two frequencies on Sgr A* . We observed 43 and 22 GHz on 2007 April 2 and 43 and 14 GHz on April 10. We changed the receiver every 20 seconds, yielding an on-source time of ~ 10 seconds for each frequency. The observations were interrupted three times by 20 minute observations of four different quasars, including the fringe-finder 3C 345. All data were correlated with 16 spectral channels per band and an integration time of one second. The total observing time including the quasars was 6 hours for each observation.

The VLBI data were edited and calibrated using standard techniques in AIPS. First, we applied the latest values of the Earth’s orientation parameters. A-priori amplitude calibration was applied using system temperature measurements and standard gain curves. We performed a “manual phase-calibration” using the data from NRAO 530 or 3C 345 to remove instrumental phase offsets among the three frequency bands. Then, we fringe fitted the data from Sgr A* using only the five inner VLBA antennas (PT, KP, FD, OV, and LA). Then, we discarded all data with elevations below 15° and performed one round of phase self-calibration on Sgr A*. Finally, we divided the calibrated *uv*-data by a model described in Bower et al. (2004), i.e. an elliptical Gaussian component of 0.71×0.41 mas with a position angle of 78° . Lightcurves were extracted from the *uv*-data with the AIPS task DFTPL.

2.4. CSO: 350 μ m, 450 μ m & 850 μ m

Nightly observations of Sgr A* were made at three wavelengths over the period 2007 April 1–6 UT, using the SHARC-II camera. The observations on April 1–5 were made with the SHARP imaging polarimeter module installed (Li et al. 2008), using the 350 μ m half-wave plate. The observing bands (selected by a cryogenic filter) were 450 μ m on April 1–3 and 350 μ m on April 4–5. The observations on April 6 were made at 850 μ m with SHARP removed from the optical path.

In this paper, we report only the total intensity measurements. Because SHARP is a dual-polarization instrument, and because the observations were made over cycles of half-wave plate angles that fully modulate the polarization, our total intensity results are insensitive to the polarization of the source.

Except for the stepping of the polarimeter half-wave plate between integrations, the observing and analysis method was similar to past CSO observations (Yusef-Zadeh et al. 2006a, 2008). We used Lissajous scans with typical full amplitudes of $100''$ in both azimuth and elevation. The instantaneous field of view is $57'' \times 57''$ in polarimeter mode and is $154'' \times 58''$ without the polarimeter.

The measured beam sizes were $8.4''$ at $350\ \mu\text{m}$, $10.1''$ at $450\ \mu\text{m}$, and $18.8''$ at $850\ \mu\text{m}$. We used the Dish Surface Optimization System (DSOS) on April 1–5. Three quadrants were working fully during the run, but the fourth quadrant of the system was available for only part of the run. For observations at the elevation of Sgr A*, we expect no significant effect on the results from the non-operational quadrant. Any change in the beam FWHM due to the status of the DSOS quadrant was less than 3%.

Mauna Kea weather conditions were good overall during the April 1–6 campaign. Occasional thin cirrus was observed visually and on satellite photos on April 3, 4, and 6; otherwise skies were clear. Local humidity was $< 30\%$ during the observations. The wind speed for April 1 was noticeably high (roughly 30 mph), but less than 20 mph on the other nights. The zenith atmospheric opacity at 225 GHz was marginal for observations at $450\ \mu\text{m}$ on April 1 ($\tau_{225} \approx 0.07$), as well as at $850\ \mu\text{m}$ on April 6 ($\tau_{225} \approx 0.15$), and rising in both cases. Atmospheric opacity on April 2–5 was excellent and relatively steady, ranging from 0.03 to 0.06 at 225 GHz.

In producing the light curves for this paper, we reconsidered the image registration and absolute calibration for all of our CSO observations of Sgr A* from 2004 September through 2008 May. The absolute pointing of the images is based on hourly measurements of point-like calibration sources, such as planets, and the pointing model for the telescope. This procedure appears to average down in a reasonable manner. The $350\ \mu\text{m}$ and $450\ \mu\text{m}$ position that we measure for the variable component of Sgr A* is within $0.3''$ of the nominal position of $\alpha_{2000} = 17^h : 45^m : 40^s.03$, $\delta_{2000} = -29^0 : 00' : 28''.1$. The agreement at $850\ \mu\text{m}$, at which the telescope beam size is larger, is somewhat worse at $0.9''$.

At any particular point in time, the telescope pointing model has only $\sim 2''$ accuracy. Therefore, we shifted the individual observations to align with the average of all the observations, using the bright dust emission in the images as the reference. Subsequent photometry of Sgr A* assumes a fixed position and beam size.

Minor changes have been made to the absolute calibration scale factor and Sgr A* “zero point”, including data which have been published in the past (Yusef-Zadeh et al. 2006a, 2008; Marrone et al. 2008). For the scale factor, we have adopted the following brightness temperatures for calibration at 350 , 450 , and $850\ \mu\text{m}$, respectively: Callisto (128, 122, 120 K), Neptune (61, 66, 81 K), and Uranus (64, 70, 86 K), arranged in decreasing order of usage and with an estimated 10% uncertainty. These brightness temperatures are not significantly different from our past assumptions. The zero point relates to the difficulty of measuring the total flux of Sgr A* with $\sim 10''$ resolution because of confusion from surrounding dust emission. We estimate an additive uncertainty of 1 Jy in our measurements of the absolute flux at $350\ \mu\text{m}$ and $850\ \mu\text{m}$, and an additive uncertainty of 0.5 Jy at $450\ \mu\text{m}$. To be consistent with the results published in this paper, the August–September 2004 measurements at $850\ \mu\text{m}$ reported by Yusef-Zadeh et al. (2006a) should be shifted upwards by ~ 0.2 Jy; the $450\ \mu\text{m}$ measurements for the same period are essentially unchanged. The $850\ \mu\text{m}$ measurements for July 2006, reported by Yusef-Zadeh et al. (2008) and (Marrone et al. 2008), should be shifted upwards by ~ 0.5 Jy. The $350\ \mu\text{m}$ results for July 2005, reported by (Marrone et al. 2008), should be shifted upwards by ~ 0.4 Jy; the $450\ \mu\text{m}$ and $850\ \mu\text{m}$ results for the same period are essentially unchanged.

2.5. SMA: 230 GHz

The SMA observed Sgr A* on the nights of 1, 3, 4, and 5 April 2007, typically covering the interval 1200–1830 UT. On the first three nights the array was tuned to observe 231.9 (221.9) GHz in the upper (lower) sideband, while on the last night the frequency was tuned to 246.0 (241.0) GHz. The array was in its “compact-north” configuration, resulting in angular resolution of approximately 3". All eight antennas were used except on April 4, when one was lost to an instrument problem. The SMA polarimetry system (Marrone & Rao 2008) was used in these observations to convert the linearly polarized SMA feeds to circular polarization sensitivity, which prevents confusion between linear polarization and total intensity variations.

The data were gain calibrated using the quasar J1733–130, which was observed approximately every 10 minutes. The absolute flux density scale was derived from observations of Callisto and has an uncertainty of 10%. To remove the effects of the extended emission that surrounds Sgr A*, only projected baselines longer than 20 k λ were used in the light curve determination. Flux density measurements were made by applying the quasar gains to the Sgr A* data, removing the average phase on Sgr A* in each light curve interval via phase self-calibration, which reduces the effect of baseline errors and phase drifts on the measurement, and fitting a central point source to the calibrated visibilities. Errors in the flux density account for thermal noise, as well as the time-variable uncertainty in the gain, which is estimated from the data themselves.

2.6. IRAM-30m Telescope: 240 GHz

Observations with the IRAM-30m telescope at Pico Veleta, Spain, were carried out on 2007 April 1–4. Because of the low elevation of Sgr A* at Pico Veleta, gain drifts due to atmospheric fluctuations are the most severe limitation to accurate flux monitoring. For the same reason, accurate peak-up is important if flux variations are to be measured that are small with respect to the quiescent flux. To account for both requirements, we alternated between Sgr B2 and Sgr A* with the following procedure, applying a wobbling secondary mirror to remove the 240 GHz emission from the atmospheric and from extended ($> 70''$) source structure. First, we pointed at Sgr B2 and measured the position of its point-source component by fitting simultaneously a Gaussian and a linear baseline (for a refined removal of extended emission) to the pointing subscans taken in on-the-fly mode (two in azimuth direction, two in elevation). The positional correction was entered and the procedure repeated to recover the correct flux. We used either the azimuth or elevation subscan, depending on where the flux was larger (and thus a better peak-up was provided). Then the antenna was moved to Sgr A*, where the same procedure was repeated. Thus, for each time sample, there are two data points representing the flux of Sgr A*, one from the pointing, and another one from the peaked up pointing. Both results were used if the pointing correction was sufficiently small. Error estimates were made by comparing the results of subscans in the same direction. To avoid effects due to instrumental and atmospheric gains drifts, only scaled fluxes of Sgr A* were retained for further analysis, using Sgr B2 as a non-variable flux reference. Data reduction was done with the MOPSIC software package¹⁹ The average Sgr B2 flux density is estimated to be 38.0 ± 1.2 Jy and was derived using the HII region G10.62-0.38 as absolute flux reference. The beam FWHM is $11''^2$.

¹⁹<http://www.iram.es/IRAMES/mainWiki/CookbookMopsic>

2.7. SMT: 250 GHz

Observations were undertaken at the SMT located at 3200m altitude on Mount Graham in eastern Arizona Baars et al. (1999) using the 250 GHz channel of the facility’s four color bolometer Kreysa (1990). This bolometer was used to observe at 250 GHz with a broad band, ranging between 200 and 290 GHz on 2007 April 1–4. We made use of the telescope’s beam switching mode, chopping horizontally $\pm 2'$ with the subreflector at a rate of 2 Hz along with an “off-on-on-off” observing mode that shifted the position of the telescope every 10 seconds to remove any asymmetries in the observations due to the chopping. Jupiter, Saturn, and Mars were used for focus and pointing references confirming the telescope’s typical half power beam width at these frequencies of $30''$ and pointing accuracy of $2''$. While Jupiter was used to set the gain of the bolometer and skydips to find the atmospheric opacity, NRAO 530, 1757-240 and G34.3 were also observed throughout the observations as secondary calibrators to check the stability and repeatability of the measurements. Finally, after splitting the data into 80 second increments (consisting of two iterations of the 40 second long “off-on-on-off” observing mode), the raw data were reduced using a version of the standard GILDAS NIC reduction program customized for the four color bolometer. Because a single calibrator was not used continuously during the first two days of observations, the flux variation of Sgr A* was uncertain and thus the data are not presented here.

2.8. NMA: 150 & 230 GHz

Interferometric NMA observations were carried out simultaneously at 90 and 102 GHz in the 3-mm band, and simultaneously at 134 and 146 GHz in the 2-mm band with bandwidth of 1024 MHz on 2007 April 1–4. The 2 and 3 mm flux densities are measured to be 1.8 ± 0.4 and 2.0 ± 0.3 Jy, respectively. The light curves of data from April 3 and 4 are presented using five and six antennas, respectively. The weather was bad on April 1 and 2 so we discarded the data on the first days of observations. 1744-31 (J2000) was used as the phase calibrator and the data was binned every 3-4 minutes. The flux measurements of Sgr A* were estimated by fitting a point source model in the uv plane restricted to distances > 20 k λ , in order to suppress the contamination from extended components surrounding Sgr A*. The FWHM of the synthesized beam in the 2mm observation on 2007, April 4 is $6'' \times 1.4''$. We used 3C279 as a passband calibrator and Neptune as the primary flux calibrator.

2.9. CARMA: 94 GHz

Interferometric CARMA observations were done to observe Sgr A* on 2007, April 2-5. Observations were made at 94 GHz using nine 6m diameter BIMA and six 10m diameter OVRO antennas with the exception of observations on 2007, April 3 which did not include any OVRO antennas. In all days, Uranus was used as the primary flux calibrator, 1744-312 as the complex gain calibrator and 1751+096 was used as a passband calibrator. The weather was poor for observing at 94 GHz on the first half of 2007, April 3 and the second half of 2007 April 4. We did not include the data during these times. Five frequency windows, each 469 MHz wide, were used at frequencies from 94 to 100 GHz. We used NRAO530 (1730-130) to cross calibrate 1744-312, in order to independently track the amplitude stability of 1744-312. All calibration was done using MIRIAD package and calibrated visibility data for each day were read into AIPS and the DFTPL task was used to extract

light curves for the source.

2.10. GMRT: 1.28 GHz

We observed Sgr A* using Giant Meterwave Radio Telescope (GMRT) in 1280, 610 and 325 MHz frequencies with central observation time on MJD 54195.0, 54191.1 and 54190.1 (5.0 April, 1.1 April and 31.1 March 2007 UT) respectively. GMRT²⁰ consists of thirty fully steerable parabolic antenna array, where fourteen antennas are randomly distributed in 1 km area and rest of the sixteen antennas are placed in three arms, spread over 25 km area, forming nearly a shape like ‘Y’. The diameter of each antenna is forty five meter. Observation band-width in each frequency was 32 MHz and integration time was 16.9 second. The source was observed for 6.1, 4.2 and 7.0 hr in 1280, 610 and 325 MHz respectively. We have done flux calibration using 3C286 and 3C48 and used Baars et al. (1977) for setting flux density scale. J1830-360 was used as phase calibrator. The bad data and radio frequency interferences (RFIs) are eliminated from the data set and the source is self-calibrated. The original data has channel width of 125 KHz in the spectral line mode. To take care of effect of the band width smearing in low frequency, we did not averaged all the channels after calibration but averaged 32, 16 and 8 channels in 1280, 610 and 325 MHz respectively (forming effective channel width of 4, 2 and 1 MHz in 1280, 610 and 325 MHz). The images are corrected for the beam-shape. Because of the strong emission from the nonthermal emission surrounding Sgr A*, the light curve of Sgr A* could have not been obtained reliably at these low frequencies 330, 630 and 1280 MHz. This is mainly due to the instantaneous elongated beam shape which contains extended structures surrounding Sgr A*.

3. Light Curves: Individual Telescopes

The results of XMM and VLT observations in X-ray and NIR have already been presented elsewhere (Porquet et al. 2008; Dodds-Eden et al. 2009). A detailed account of INTEGRAL observations are given elsewhere (Trap et al. 2009). To present all the data that were taken during this campaign, we include the XMM and VLT light curves again here and briefly review the results of these observations that have already been published elsewhere.

3.1. NICMOS Photometric Measurements

Figure 2a shows the observed variability of Sgr A* in the NICMOS 1.45 and 1.70 μ m bands, where there is good agreement between the two bands. The observed “quiescent” emission levels of Sgr A* in the 1.45 and 1.70 μ m bands are ~ 32 and ~ 38.5 mJy, respectively, but some fraction of this total signal is due to the neighboring star S0-2. During flare events, the emission is seen to increase by anywhere from a few percent to 25% above these levels. In spite of the somewhat lower signal-to-noise ratio for the 1.45 μ m data, due to the somewhat lower sensitivity of the NICMOS detector and increased effects of extinction, the flare activity is still easily detected in this band. In order to confirm that the observed variability of Sgr A* is not due to either instrumental or data reduction effects, we have compared the Sgr A* light curves to that of the star S0-2 and to a

²⁰www.gmrt.ncra.tifr.res.in

region of background emission with the NICMOS images, as shown in Figure 2b. The photometric measurements for Sgr A* show obvious signs of variability in six of the seven windows of HST observations, while the corresponding light curves of S0-2 and the background remain quite stable.

The panels of Figure 3a-e present detailed light curves of Sgr A* and, for comparison, S0-2 for each of the seven HST observing windows. These plots show the time-ordered measurements in the 1.45 and 1.70 μm bands, where we have now subtracted the mean “quiescent” flux level, leaving the net variations in emission for both Sgr A* and S0-2. All light curves are aperture and extinction corrected. Each observing window consists of 5 to 7 HST orbits, with each orbit covering ~ 46 minutes. We have identified flaring activity in at least one orbit in each of the seven observing windows. These activities are identified in the light curves with labels designating the day (1–7) and the flare even within the day (A–C). A typical flare event lasts between 10 and 40 minutes. The amplitudes and durations of the events are similar to what was found in our earlier HST observations (Yusef-Zadeh et al. 2006a).

To examine the short time scale variability in more detail, the 1.70 μm light curves are shown in Figure 4 with a sampling of 64 seconds. The Sgr A* and S0-2 light curves are qualitatively similar to those in Figure 3, except for the finer sampling and we show only the 1.70 μm band because the 1.45 μm data do not have sufficient signal-to-noise in this shorter integration period. There are 16 identified flaring events, all of which are shown in 45min periods in two panels of eight flares. One type of fast fluctuation that we have detected is generally associated with the rise or fall of bright flares, or at the peaks of bright flare emission, as seen for the flares 1A, 2A, and 5A. Similar minute time-scale variability has also been detected by Dodds-Eden et al. (2009). Another type of fluctuation is the point-to-point variability seen during some of the quiescent phases of low-level of activity, such as flares 1B, 1C, 2B, 3A, 4B, 6A, and 7A.

3.2. VLT NIR and Mid-IR Observations

The VLT observations used multiple bands to observe Sgr A* on 2007 April 1–7, using the two instruments NACO (NIR) and VISIR (mid-IR). The results of these observations, which included the identification of seven flaring events are discussed in detail by Dodds-Eden et al. (2009). The brightest flare detected at 3.80 μm coincides with the brightest X-ray flare on April 4. Figure 5 shows a composite light curve of VLT observations with labeled flares using 3.8 μm , 2.12 μm and 1.66 μm NIR bands. No NIR spectral index measurements are available for the detected flares. However, a 3σ upper limit of 57 mJy is placed at 11.88 μm for the bright 3.8 μm flare on April 4 with a peak flux density of ~ 30 mJy (see also Trap et al. 2009). The brightest NIR flare detected in this campaign consists of a cluster of overlapping flares that last for about two hours. The second brightest flare detected by the VLT is identified as #6 in Figure 5. This flare precedes the bright NICMOS flare 5A (April 5), as shown in Figure 3e. These flares are components of another period of flaring activity lasting for about two hours.

3.3. X-ray Flaring Activity

The X-ray light curves between 2 and 10 keV with a time binning of 144s are shown in Figure 6. A total of five flares were observed: one in 2007 April 2 (labeled #1) with a peak X-ray luminosity $L_{2-10\text{keV}} = 3.3 \times 10^{34}$ erg s $^{-1}$ and four on 2007 April 4 (labeled #2, #3, #4, #5) with peak

$L_{2-10\text{keV}}=24.6, 6.1, 6.3, \text{ and } 8.9 \times 10^{34} \text{ erg s}^{-1}$, respectively (Porquet et al. 2008). For the first time, within a time interval of roughly half a day, an enhanced incidence rate of X-ray flaring was observed, with a bright flare (#2, with a duration of 2900 s) followed by three flares of more moderate amplitude (#3, #4, #5, with durations of 300, 1300, and 800 s respectively). An enhanced rate of X-ray flares, although with lower amplitudes, was also reported in Belanger et al. (2005) when one moderate and two weak flares were detected within a period of eight hours. These rates of X-ray activity (Porquet et al. 2008; Bélanger et al. 2005) are clearly higher than the typical duty cycle of one X-ray flare a day (Baganoff 2003). The brightest event on 2007 April 4 represents the second-brightest X-ray flare from Sgr A* after the X-ray flare with $\Gamma = 2.2 \pm 0.3$ on 2002, October 3, on record with a peak amplitude of about 100 times above the 2–10 keV quiescent luminosity²¹ This bright X-ray flare exhibits similar light-curve shape (i.e., nearly symmetrical), duration (~ 3 ks) and spectral characteristics to the very bright flare observed on 2002, October 3 with XMM-Newton (Porquet et al. 2003). Its measured spectral parameters, assuming an absorbed power law model including the effects dust scattering, are $N_{\text{H}} = 12.3_{-1.8}^{+2.1} \times 10^{22} \text{ cm}^{-2}$ and $\Gamma = 2.3 \pm 0.3$ where the quoted errors are at the 90% confidence level. Therefore, the two brightest X-ray flares observed so far from Sgr A* exhibited similar soft spectra $\Gamma \sim 2.2 - 2.3$. The spectral parameter fits to the sum of the three following moderate flares, while lower ($N_{\text{H}} = 8.8_{-3.2}^{+4.4} \times 10^{22} \text{ cm}^{-2}$ and $\Gamma = 1.7_{-0.6}^{+0.7}$), are compatible within the error bars with those of the bright flares. However, fixing the column density at the value found for the brightest flare (i.e. $N_{\text{H}} = 12.3 \times 10^{22} \text{ cm}^{-2}$) leads to a larger photon index value for the sum of these moderate flares, i.e. $\Gamma = 2.1 \pm 0.4$.

3.4. 43 GHz Time Variability: VLA

Figure 7a,b shows light curves measured during April 1–4 at 43 GHz with the VLA, using 87sec and 300 sec sampling, respectively. The light curve of the phase calibrator 17444-31165, which itself is cross calibrated by NRAO530, is flat and is shown at the bottom of each panel in Figure 7a. Since NRAO530 is not the primary calibrator, it provides a second check on instrumental stability and that its light curve was flat also.

The light curves of Sgr A* show variations on a variety of time scales from as short as 30 min to longer than five hours at 43 GHz. The fluctuations on time scales of several hours $\sim 5 - 6$ hours can be seen in Figure 7a,b. The slow flux variation over 5-6 hours could, in principle, result from the contamination of the emission by an asymmetric distribution of extended structures surrounding Sgr A* especially when a compact configuration of the VLA is used. However, the contamination of flux by extended emission is minimal for uv data $> 90k\lambda$ (or $2.3''$) and the variability on several hour time scale is intrinsic to Sgr A*. Previous high resolution data taken with a wide configuration of the VLA have also shown the presence of flux variation of Sgr A* on such time scales (Yusef-Zadeh et al. 2006a,b and 2008). The contamination of extended emission was clearly seen at low elevations in the uv data $< 90k\lambda$ at 43 GHz, and our 22GHz data taken simultaneously with 43 GHz data on 2007 April 1-4 were useless for time variability analysis because of the limited uv range (i.e., $< 70k\lambda$).

Most of the power of the 43 GHz fluctuations in four consecutive days of observations appears to fall in a range between 30 minutes and few hours, as best shown all light curves of Figure 7b. For

²¹No detection was made using INTEGRAL in the 20–40 keV and 40–100 keV energy bands, leading to 3σ upper limits of 2.63 and $2.60 \times 10^{35} \text{ ergs s}^{-1}$, respectively (Trap et al. 2009).

example, fluctuations with ~ 1 h time scale are detected at a level of 200 mJy in the April 1 and April 2 light curves centered near 13h and 11:15h UT, respectively. The light curve of April 4 shows largest flux variations at a level of $\sim 40\%$ are seen to increase flux density from 1.1 Jy at 9h UT to 1.6 Jy near 15h UT. Another interesting feature of the April 4 light curve is the presence of multiple weak fluctuations at a level of 50 mJy on a time scale of ~ 20 -30 minutes. Figure 7c shows the light curves of April 4 for simultaneous observations at frequencies of 43.1851 GHz and 43.5351 GHz with a 30sec sampling time. The frequency separation between these light curves is 345 MHz. We note at least five 20–30 minute fluctuations that are seen in both light curves. A more detailed account of the power spectrum analysis of the time variability of Sgr A* in radio wavelengths will be given elsewhere.

3.5. 14, 22 and 43 GHz Time Variability: VLBA

Figure 8a shows 43 GHz light curves based on VLBA observations on April 1, 5 and 11, with a 60 sec sampling time. Figure 8b shows the light curves at 22 GHz and 43 GHz on April 2 whereas Figure 8c shows the light curves at 15 GHz and 43 GHz on April 10. The flux density of Sgr A* show variations on several hour time scales in these VLBA observations at multiple frequencies. These light curves show the first measurements of the flux variation of Sgr A* on a VLBA (milli-arcsecond) scale at several frequencies.

Fluctuations in phase coherence and amplitude errors could produce significant changes in flux on short timescales. However, it is unlikely that calibration errors are similar at two frequencies, thus the flux variation on ~ 5 -hour time scale (Fig. b,c) is intrinsic to Sgr A*.

3.5.1. 43 GHz Light Curve: VLBA and VLA Comparison

Because VLBA and VLA measurements on April 1 and 2 are taken simultaneously at 43 GHz, we compared the two light curves, as shown in Figure 9a,b with a 300 sec sampling time, respectively. The comparison of the light curves examines directly the localization of flaring events at radio wavelengths. The largest fluctuations in both VLA and VLBA light curves appear to agree with each other. Peaks with hourly time scale durations occur in both light curves near 13h UT on April 1, as seen in Figure 9a. Similarly, the slow decreasing trend in the flux of Sgr A* over few hours is seen in the light curves of 2007 April 2 at 43 GHz using both the VLA and VLBA, as shown in Figure 9b. The behavior of the light curves on hourly time scales measured with VLBA provides the first direct evidence that flaring activity arises from the innermost region of Sgr A* on milliarcsecond (mas) scales. The size of the flare emission is dominated by interstellar scattering. The general agreement between the VLA and VLBA light curves imply that flaring region that has been detected is unresolved with the VLA.

There are also discrepancies between the two light curves. One is the different values of “average levels” of flux taken in the light curves measured with the VLA and VLBA. In all the measurements shown in Figures 7a and 8a,b the average-level of VLBA flux appears to be lower than that of the VLA by ~ 200 mJy. The second discrepancy is the flux variations do not agree with each other on small time scales in VLA and VLBA light curves. The uncertainty in the absolute flux density calibration of Sgr A* at 43 GHz using VLBA and VLA could easily explain the first discrepancy. It is possible that the emission from Sgr A* could be contaminated by extended emission from the

surrounding medium, as measured with the VLA, even though we have selected data with $uv > 100k\lambda$. This could explain why the VLA and VLBA light curves do not agree with each other on 10-15 minute time scales. Lastly, it is possible that these discrepancies could be explained by a core-halo structure of emission from Sgr A* in which the halo component is resolved out in VLBA observations. Future simultaneous VLA observations using its most extended array configuration and VLBA should be able to examine closely the reason for these discrepancies.

3.6. CSO 350 μ m, 450 μ m, 850 μ m Light Curves

Figure 10 shows the light curves at three submillimeter wavelengths. The data have been smoothed to increase the signal-to-noise ratio with a sampling time of ~ 6.5 minutes. As at radio wavelengths, the flux of Sgr A* appears to be varying on hourly time scales. The largest Sgr A* increase is detected at the beginning of the observation near 13:30 UT on 2007 April 1. These light curves show evidence for hourly and intraday variability at 450 μ m, at a level of 14%. The mean daily flux of Sgr A* at 450 μ m is $\sim 3 \pm 0.25$ Jy.

Figure 10b shows some of the first variability of Sgr A* at 350 μ m. The flux increase on 2007, April 4 over 5 hours is about 50% of the initial flux of Sgr A*. This steady increase of flux density over several hours is seen to continue at 90 GHz (see section 3.10). Figure 10c shows the light curve at 850 μ m on 2007, April 6. Unlike the other submillimeter light curves shown here, this light curve appears to show time variability on a time scale of ~ 10 minutes as seen near 13h:20m UT. Such sharp variations, though with low signal-to-noise values, at 850 μ m at such a short time scale resembles the recent light curve obtained with a different instrument (LABOCA of APEX) (Eckart et al. 2008). The reality of such a short time scale variation needs to be confirmed.

3.7. SMA: 230 GHz Light Curves

Figure 11 shows the light curves taken from four days of observations with the SMA at 230 GHz. The 2007 April 1 data shows an asymmetric profile indicating a duration of possibly ~ 4 hours considering that there is a gap between 16h and 17h:30m UT. Similar submillimeter characteristics have been seen recently at 850 μ m (Yusef-Zadeh et al. 2008). The 2007 April 3 light curve shows an emission peak near 14h UT, before a slow decay that lasts for about 4 hours. The light curve obtained with SMT on the same day and at the same wavelength showed the rising part of the light curve suggesting that the duration of the flare on this day could be as long as 8 hours. The 2007 April 4 light curve shows a typical profile of submillimeter flare emission, except for a dip in the flux at a level of 100 mJy near 14h UT. The April 5 data shows a light curve with multiple peaks as the light curve decays. The typical time scale for this variation is between ~ 1 -2 hours. The overall percentage of flux variation during 6 hours of observations is between 10% and 30%.

3.8. SMT 250 GHz Light Curves

The SMT light curves of Sgr A* and calibrators (in blue) for 2007, April 1-4 are shown in Figure 12. Because SMT and SMA observed Sgr A* at the same wavelength considering the broad bandwidth of the SMT, we compared the SMT light curves with those of SMA on April 1, 3 and 4. An increase in flux of ~ 1 Jy in the rising part of the light curve is seen between 10h UT and 14h UT on 2007,

April 3. This increase is similar to the decrease in the flux of Sgr A* found in the decaying part of the SMA light curve, as seen in Figure 11.

The low spatial resolution of the SMT results in a higher background level for the Sgr A* light curve. The discrepancy in the zero level flux of Sgr A* using SMT and SMA on April 3 and 4 is due to the fact that the emission from Sgr A* using SMT is contaminated by 3.5 ± 0.2 Jy of flux from extended features. If this flux is subtracted from the April 3 data and combined with the SMA light curve, the duration of the variability is estimated to be ~ 6 hours.

The 2007, April 1 shows the most dramatic flux variation of ~ 2 Jy. The reality of this feature can not be confirmed as different calibrators were used at the beginning of the observation. However, a 3.6 ± 0.2 Jy subtraction from the SMT data matches well with the SMA data, thus suggests that the sudden rise 11h UT is likely to be real.

3.9. IRAM 240 GHz Light Curves

Figure 13 shows the light curves of the two days of IRAM observations on 2007 April 3 and 4. There is no evidence for any flux variations in these observations. The April 4 light curve overlaps with the biggest NIR/X-ray flare detected during this campaign. However, there is no indication that the 240 GHz flux density changed by more than 1.5 ± 0.5 Jy between 5h and 7h UT, during which the bright NIR/X-ray flare took place.

3.10. NMA 140 GHz and 230 GHz Light Curves

Figure 14 shows the NMA light curves of Sgr A* and 1744-312 based on two days of observations under excellent weather conditions. The flux of the calibrator remains flat during these observations, whereas the flux of Sgr A* increases by ~ 0.5 Jy at 90 GHz on April 3. The April 4 light curve shows a slight increase at 146 GHz before decaying strongly by more than 1 Jy. The duration of the flare is roughly 2 hours.

3.11. CARMA Light Curves

Fig 15 shows the light curves of Sgr A* and the calibrator 1733-130 at 94 GHz taken for four days of observations on 2007, April 2-5. There is flux variation on short and long time scales in all days of observations. There is concern on the variation of the calibrator evident in almost all days of observations. Due to this uncertainty, we compared the light curves with other 94 GHz and 43 GHz measurements and we believe the large scale variation may reflect the intrinsic variable emission from Sgr A*. However, the flux variation of Sgr A* on short time scale may not be valid.

3.12. GMRT Light Curves

As we observe Sgr A* at long wavelengths, the light curve of Sgr A* may be contaminated by the extended nonthermal emission surrounding Sgr A* as well as by interstellar scattering which becomes more important at long wavelengths. In order to avoid the contamination by extended emission, we used the uv data at the highest elevation as well as restricted the uv distribution

be greater than $80k\lambda$. Also, interstellar scintillation is expected to operate on longer time scales than hourly time scales that we are sensitive to. A flux variation of ~ 80 mJy over four hours was detected. Given the limited resolution of the GMRT data at this frequency, it was not clear if this variation reflects the flux of Sgr A* at 1.28 GHz or an artifact of the contamination of extended flux. It is clear that higher resolution data are needed to separate Sgr A* from the extended features in its vicinity.

4. Analysis

4.1. NIR Flare Statistics

Given the ability of HST to produce continuous observations over many 45 min orbital visibility periods, along with its long-term photometric stability, the NIR NICMOS data provide an excellent way to investigate the flare strength distribution over many flare episodes. Figure 16 shows a histogram of the NICMOS $1.70\mu\text{m}$ net flare emission for the 7 days of data obtained in this campaign. The net flare emission is measured by first subtracting the background emission for each day before the excess flux above the background is selected. Thus, the selected data points do not sample the peak flare emission but rather the flux associated with flaring activity. The peak of values centered at a net flux of zero represents the emission from Sgr A* during “quiescent” periods. The positive half of the histogram, on the other hand, shows a tail of flare emission events extending out to ~ 10 mJy. The “quiescent” distribution is best fitted with a Gaussian, which is expected from the level of random noise in the observations. The tail of flare emission can be fitted with a power-law distribution having an index of -1.19 ± 0.27 and a low-energy cutoff at $S_\nu = 1$ mJy. The dotted line in the figure shows the result of simultaneous Gaussian and power-law fits to these two components.

Yusef-Zadeh et al. (2006a) reported that distribution of flare activity seen in our more limited 2004 NICMOS observations could be fitted by two simultaneous Gaussian profiles. A reanalysis of those data, however, now show that a power-law distribution with a low-energy cutoff yields a good fit to the 2004 epoch data as well. Figure 17 shows a histogram of the 2004 $1.60\mu\text{m}$ data, with Gaussian and power-law fits to the two components shown by the broken lines. The best power-law fit to these data has an index of -1.11 ± 0.13 , with a low-energy cutoff of $S_\nu = 0.25$ mJy. This is remarkably consistent with the best-fit power-law index of the 2007 data. We note that the fraction of observing time that flare activity has been detected in the 2004 and 2007 campaigns is $\geq 32\%$ and $\geq 37\%$, respectively.

The NIR flare histograms for the two epochs show that the probability of measuring flux S_ν at any instant is approximately proportional to $1/S_\nu$. Presumably this reflects the statistics of the flaring behavior of Sgr A* at NIR wavelengths. To explore this we construct a simple phenomenological model for the flaring by simulating a light curve and then sample it to construct a simulated histogram. This model shows that the observed $1/S_\nu$ behavior arises quite naturally, but does constrain the statistics of the flaring.

Our phenomenological model represents the flaring as a sequence of 100 Gaussian profiles occurring over 100 arbitrary time units, with flare i characterized by peak flux S_i , timing of the peak t_i , and standard deviation of the flare σ_i , so that the net light curve may be written as

$$S_\nu(t) = \sum_{i=1}^{100} S_i \exp\left(-\frac{(t-t_i)^2}{2\sigma_i^2}\right). \quad (1)$$

The parameters S_i , t_i , and σ_i are drawn randomly and uniformly from the ranges $[0, 1]$, $[0, 100]$ and $[0, \sigma_{\max}]$, respectively, and the resulting light curve is evenly sampled every 0.2 time units to create a flare histogram. Note that σ_{\max} is the only independent parameter of this model, as increasing the number of flares and changing the maximum flare amplitude can be accommodated by rescaling the flux and time units. In addition, changing the sampling rate or the number of flares does not affect the statistics, provided that the light curve has already been adequately sampled (which is the case for our adopted sampling rate of 50 per time unit). We find that $\sigma_{\max} \lesssim 0.5$ yields the observed $1/S_\nu$ behavior.

A typical simulated light curve and the corresponding histogram for $\sigma_{\max} = 0.5$ are given in Figures 18a and b, respectively. The slope of S_ν^{-1} is drawn on Figure 18b. Larger values of σ_{\max} lead to significant overlap between flares, tending to give a flatter dependence of the flux probability on S_ν . This does not, of course, prove definitively that the flares behave as given by equation 1. Other choices of functional form or different statistics for S_i may also yield the $1/S_\nu$ behavior of the histogram. It does, however, seem to require that the flare events do not significantly overlap each other.

4.2. Spectral Index Distribution Between 1.45 μm and 1.70 μm

We have constructed a log-log distribution of spectral index based on the NICMOS 1.45 μm and 1.70 μm data. Figure 19 shows the "color" distribution of all the data selected with signal-to-noise $S/N=3$. The diagonal line (in red) shows the spectral index of $\beta=0.6$, where $F_\nu \propto \nu^{-\beta}$. For comparison, β of -4, -2, 2, and 4 are also plotted. This figure shows a tendency for the spectral index of low flux values to be steeper than 1, whereas the high flux values are represented by a flatter distribution of spectral index. Because the data points used in making Figure 19 are not taken simultaneously at the two different wavelengths, we attempted to estimate spectral index values of adjacent data points, where the flux of Sgr A* is not varying rapidly, such as during the fast rise or fall of individual flares. The 1.45 and 1.7 μm NICMOS images were acquired back-to-back in long sequences, in which the exposures within each pair are separated in time by about 2.5 minutes. The points shown in Fig. 19 represent all adjacent pairs of measurements (adjacent meaning ~ 2.5 minute separation) for which the S/N in the individual measurements is greater than 3 (hence not all available pairs from Fig. 3 are included). The fact that the overall Sgr A* flux could be changing within that 2.5 minute time scale is a concern and is why the spectral index values listed in Table 1 were taken from only those measurements where we could see from the light curves that the overall Sgr A* flux was not changing much on that ~ 2.5 minute time scale. The full light curves also indicate that the overall flux of Sgr A* does not often change on such short time scales and therefore the number of suspect measurements in Fig. 19 should be a relatively small fraction of all measurements. Hence we only deduce general trends from that diagram.

We identified five sets of data points associated with five different flares during which the overall Sgr A* flux is not varying rapidly. Table 1 shows the corresponding flux and spectral index values using data sampled at 144 sec intervals. The two brightest flares, 5A and 2A, have spectral indexes 0.73 ± 0.16 and 0.97 ± 0.27 , whereas the weaker flares have indexes steeper than $\beta=1.5$. These individual measurements are consistent with the spectral index trend shown in Figure 19. We also find that the spectral index of the brightest flares are consistent with recent Keck measurements, which yield a spectral index of 0.6 (Hornstein et al. 2007). The spectral index of low flux values is also consistent with VLT measurements, which show a steep spectrum for weak flares (Eisenhauer et al.

2005; Gillessen et al. 2006). These measurements suggest that the spectral index of flares varies with the NIR flare strength, support earlier measurements by Gillessen et al. (2006) and disagree with measurements by Hornstein et al. (2007) who claim a constant spectral index in NIR wavelengths. The variation of spectral index with flare emission at NIR wavelengths has important implications on the inverse Compton scattering mechanism of X-ray and soft γ -ray emission from Sgr A* (Yusef-Zadeh et al. 2006a) as well as on the hypothesis that X-ray emission is due to synchrotron mechanism (Dodds-Eden et al. 2009). It is possible that weak flares with a steep energy index of particles are associated with low-level activity of the accretion disk of Sgr A*, whereas the bright flares represent the hot magnetically-dominated events that are launched from the disk. Polarization characteristics of the weak and strong flares may constrain models of the flare emission. The correlation of the spectral index and flux has been discussed in the context of electron heating and cooling by a turbulent magnetic field (Bittner et al. 2007). In the synchrotron scenario, the higher value of the spectral index at low NIR fluxes could be an indication of the cooling break.

4.3. NIR Power Spectrum Analysis

Genzel et al. (2003) had reported a possible 17 min NIR periodicity with implications for the spin of the black hole. Our previous 2004 HST data (Yusef-Zadeh et al. 2006a) showed a marginal detection of power at 33 ± 2 minutes. We investigated the power spectrum of flare data taken with the new NICMOS measurements. We created Lomb-Scargle periodograms (Scargle 1982) to search for periodicities in our unevenly-spaced NIR measurements. We performed 1000 simulations of each light curve, with the same sampling and variance as the data, and with simulated noise following a power-law ($P(f) \propto f^{-\delta}$) chosen to match the periodogram of the data as closely as possible (following Timmer & Konig 1995, Mauerhan et al. 2005), typically with an index δ of 1.5 or 2. Artificial signals are seen at the 90 minute orbital period of HST, and the 144 second filter switching cycle, and discounted. For each point in a lightcurve, we identify the periodogram simulation at the n th (where $n=99, 99.9$) percentile of the distribution, and thus create lines below which $n\%$ of the simulations fall. Figure 20 shows the power spectrum as a solid line and the dotted lines show the the spectrum of the noise using power-law distributions. Only one HST observation shows any power above the 99.9 percentile line, on 2007 April 4, near 2 hours.

The 99.9 percentile refers to the local distribution; however, the chance of getting a point above the 99.9 percentile line must be computed considering all trials (Benlloch et al. 2001). We sample 158 frequencies above 10.8 minutes, the lower limit of our simulation software, and perform seven observations, so our total is 1106 observations, suggesting ~ 1 peak above the 99.9 percentile line. We have two adjacent points above the 99.9 percentile line, but these points are probably not independent. Altering the index δ within a range consistent with the data does not change the strength of the signal. We conclude that the significance of this possible periodicity is not particularly strong.

The lack of any significant power between 17 and 20 minutes supports the results from an earlier analysis of HST data in 2004 (Yusef-Zadeh et al. 2006a). Recent analysis of data taken with the combined VLT and the Keck observations shows no significant power on short time scales (Do et al. 2008; Meyer et al. 2008).

5. Discussion

5.1. X-ray Flare Emission Mechanism

As described in §3.3, five X-ray flares were detected in the present observing campaign. The strongest X-ray flare (#2) coincided with a strong NIR flare observed with the VLT (Dodds-Eden et al. 2003). HST observations detected three of the remaining four X-ray flares (#1, #4 and #5) corresponding to flares 2A, 4A and 4B, respectively. Figure 21a,b show the X-ray light curves of these newly detected NIR flares at $1.70\mu\text{m}$. Table 1 presents the flux and spectral index of the NIR flare 4A. The remaining X-ray flare detected in this campaign (#3) was not observed contemporaneously in the IR. The simultaneous monitoring of Sgr A* in X-rays and the IR have shown that X-ray flares are always accompanied by flaring in the IR but that the reverse is not necessarily true (Porquet et al. 2009).

The NIR flare emission from Sgr A* have been shown to be highly polarized (Eckart et al. 2006a; Meyer et al. 2006) and is therefore likely to be produced by synchrotron emission from GeV electrons in the ~ 10 G magnetic field strengths thought to be present in the vicinity of Sgr A*. The 30 minute duration of the flares is broadly in line with the synchrotron cooling time scale of these electrons. Substructure in the NIR flare lightcurves has been attributed to doppler beaming and lensing of an orbiting hotspot (Meyer et al. 2006), although this remains to be confirmed.

The X-ray flares are always seen in concert with flaring in the IR (when the IR has been simultaneously observed). Thus scenarios for the X-ray emission are directly associated with the acceleration of the GeV electrons responsibly for the IR synchrotron emission, either through upscattering of submillimeter seed photons (Markoff et al. 2001, Yusef-Zadeh et al. 2006, 2008), synchrotron self-Compton (Eckart et al. 2006a) simply as synchrotron emission from the high energy tail of the accelerated electrons (Yuan et al. 2003, Dodds-Eden et al. (2009) or from the NIR emitting electrons (Eckart et al. 2006a). Dodds-Eden et al. (2009) have recently shown that the ICS scenario requires an uncomfortably small submillimeter source size ($\lesssim R_s$) to match the observed X-ray and NIR fluxes for flare #2. In addition, although the other flares can be modeled with source sizes of a few Schwarzschild radii and field strengths in the 10 G range (e.g., Yusef-Zadeh et al. 2006), the energy density of the GeV electrons in the NIR-emitting region exceeds the magnetic energy density by more than an order of magnitude, and their acceleration and confinement becomes problematic (this is also the case for flare #2). Finally, the duration of the X-ray flare is shorter than the IR flare whereas one might expect them to be identical. Dodds-Eden et al. 2009 therefore strongly preferred the synchrotron scenario. This implies that the acceleration mechanism must continuously resupply the 100 GeV electrons for the 30 minute duration of the observed flares as the synchrotron loss time of the ~ 100 GeV electrons responsible for the synchrotron emission is ~ 30 seconds.

Here we consider an alternative ICS scenario: the upscattering of NIR seed photons emitted during the flare by the mildly relativistic ~ 10 MeV electrons responsible for the quiescent radio-submillimeter emission. If the submillimeter emission region were optically thin this would produce a similar X-ray luminosity as the upscattering of submillimeter seed photons. However, as the submillimeter source region is optically thick below 1000 GHz, the observed submillimeter flux is produced by a fraction of the underlying electrons. The emission region is optically thin to NIR photons, and so all of these electrons are available to upscatter NIR seed photons to X-ray energies. As a result, the ICS luminosity produced through this scenario will dominate that produced by the original ICS scenario.

To estimate the resulting X-ray flux we characterize the electrons responsible for the submillimeter emission by electron number density n_e , a relativistic Maxwellian energy distribution at temperature T , and a quasi-spherical region of size R . These electrons upscatter the NIR seed photons arising from synchrotron emission from the relativistic electrons producing the NIR flare with observed flux S_ν at the earth. The ICS flux depends on the direction-averaged intensity, J_ν , of seed photons which in turn depends on the location and size of the flare emission region; we estimate this to order of magnitude by simply assuming that the flare region is of similar size to the submillimeter emitting region, such that $J_\nu = (d^2/\pi r^2) S_\nu$, where $d = 8$ kpc is the distance to the Galactic center. The energy of the upscattered photons is small compared to the MeV-range of the electron energies, so we can use the Thomson scattering cross-section. To a good approximation, scattering by an electron with energy $E \gg m_e c^2$ boosts the seed photon energies by a factor $(E/m_e c^2)^2$ irrespective of the scattering angle. The differential ICS luminosity per unit energy interval is then simply

$$L(E_\gamma) = \frac{16\pi\sigma_T}{3h} \int N(E) J_\nu dE \quad (2)$$

where $N(E) dE$ is the *total* number of electrons in the energy interval $[E, E + dE]$, and J_ν is the direction-averaged intensity of the seed photons at frequency $\nu = E_\gamma/(E/m_e c^2)^2$. For temperatures in excess of a few MeV, the vast majority of the electrons have $v \approx c$, so we approximate the relativistic Maxwellian distribution by $f(E) \approx (2kT)^{-1} (E/kT)^2 \exp(-E/kT)$ and then $N(E) = \frac{4}{3}\pi R^3 n_e f(E)$. If the spectrum of the seed photons is a simple power-law, ie. $S_\nu = S_0(\nu/\nu_0)^{-\beta}$, the differential luminosity is

$$L_\gamma(E_\gamma) = \frac{32\pi\sigma_T d^2}{9h} \Gamma(3 + 2\beta) S_0 n_e R \left(\frac{E_\gamma}{E_{\gamma 0}} \right)^{-\beta} \quad (3)$$

where $E_{\gamma 0} = (kT/m_e c^2)^2 h\nu_0$.

By way of illustration we adopt reasonable choices $R = 10 R_s$, $n_e = 10^7 \text{ cm}^{-3}$, and compute the ratio of 2–10 keV luminosity to $2.2 \mu\text{m}$ flux as a function of spectral index β . The results for various adopted electron temperatures are plotted as solid curves in Figure 22. The X-ray to NIR flux ratio declines with increasing spectral index β (where $S_\nu \propto \nu^{-\beta}$ created by upscattering of optical/NIR photons from an electron population with radius $R = 10 R_s$, and uniform density $n_e = 10^7 \text{ cm}^{-3}$, and temperatures of 3, 5, 7, and 10 MeV). Because X-rays in the 2-10 keV band are produced by upscattering of photons that are shortward of $2.2 \mu\text{m}$, and for fixed flux at $2.2 \mu\text{m}$ there are less of these as β is increased. Also shown for comparison are the measured ratios and spectral indices of the 7 coincident IR and X-ray flares seen to date (Yusef-Zadeh et al. 2006; Belanger et al. 2005; Eckart et al. 2006; Hornstein et al. 2007; Marrone et al. 2008; Porquet et al. 2008; Dodds-Eden et al. 2008; this paper). The high value of β at high temperature correlates with a high ratio of X-ray to NIR flux, as shown in Figure 22. This correlation is consistent with the low flux value of NIR flare emission for high value of the spectral index, as described in section 4.2. We conclude that the fluxes of the observed X-ray flares are broadly consistent with this ICS scenario.

Our simple model predicts that the spectral indices of the X-ray and IR flares should be identical, but this not need be the case for a broken power-law electron energy distribution. In the case of the strongest X-ray flare (#2) which coincides with a strong NIR flare, the NIR spectral index and X-ray spectral index are different with $\beta_{X\text{-ray}} = 1.3 \pm 0.3$ (90% confidence) whereas $\beta_{NIR} < 1.0$ (3σ) (Dodds-Eden et al. 2009). This could be explained by a broken power law of NIR emitting electrons with a steeper spectral index shortward of $3.8 \mu\text{m}$, perhaps resulting from a shorter time scale for synchrotron cooling of electrons at high energies. In this scenario, the flux in the 2-10 keV

band is produced predominantly by upscattering of photons with wavelengths shortward of $1\ \mu\text{m}$. This may explain why the width of the bright 2007 April 04 flare is less in X-rays than in the infrared: the infrared flare may have decayed more rapidly shortward of $1\ \mu\text{m}$ than at $3.8\ \mu\text{m}$ and so the X-ray flux declines without a corresponding decrease at NIR wavelengths.

The extent of the submillimeter-emitting electron population may on occasion give rise to significant time delay between infrared flaring and their X-ray counterparts. A sufficiently hard IR flare would lead to X-ray production by inverse Compton scattering on the extended $\sim 1000 R_s$ outer envelope of low-temperature electrons, producing weak post-main-flare X-ray emission lasting for tens of minutes after the main flare has subsided. Theoretically, the electron temperature is set by a balance between heating by Coulomb interactions with protons and by plasma effects and synchrotron cooling. kT for the protons is a reasonable fraction of their virial energy because of inefficient cooling in the accretion flow. This implies that the protons should be non-relativistic at $\sim 1000 R_s$, with MeV-range energies. The electrons are likely to have similar energies because of formalization and are then mildly relativistic. Empirically, Loeb & Waxman (2007) estimate from the radio/submillimeter spectrum that the electron temperature is a few MeV all the way out to $1000 R_s$. Detection of these “echoes” would confirm the scenario proposed here and help determine the size of the outer region which is rendered inaccessible to direct by the effects of interstellar scattering in radio wavelengths.

5.2. Cross-Correlation of Light Curves

As pointed out in the previous section the adiabatic expansion picture of the flare emission from Sgr A* makes the predictions that i) the NIR and X-ray emission are expected to be simultaneous and therefore optically thin whereas optical depth effects become important at lower frequencies, thus a time delay is expected between their peak emission. To examine these issues, a great deal of data have been obtained simultaneously in this campaign, which allows us to cross-correlate the multi-wavelength data for each day of observation. The light curves that we have presented thus far indicate that the flux of Sgr A* is constantly changing as there is low-level flare activity in almost all wavelength bands. There are very few measurements that were taken simultaneously with the same time coverage with few exceptions, as described below.

The cross-correlation analyses in this paper use the Z-transformed discrete correlation function algorithm (Alexander 1997); see also (Edelson & Krolik 1988). This algorithm is particularly useful for analyzing sparse, unevenly sampled light curves. We identify the peak likelihood value, and a $1\text{-}\sigma$ confidence interval around that value, using a maximum likelihood calculation (Alexander 1997).

5.2.1. NIR, X-ray and Radio flare Emission

Altogether there are four detected NIR flares that have shown X-ray counterparts. There is no evidence that there is time delay between the peaks of any of the detected flares, thus supporting the fact that both NIR and X-ray emission are optically thin. The lack of time delay places a strong constraint on the ICS picture.

The strong flare and simultaneous coverage in both X-ray and NIR wavelengths observed on 2007 April 4 is one example in which a cross correlation peak with small error bars can be obtained. The

cross-correlation of the light curves at X-ray and NIR wavelengths is shown in Figure 23. The peak of the cross-correlation shows that X-ray emission is delayed by 29 seconds with a one-sigma error bar of -6.5 and +7.0 minutes. In the ICS picture, as described in section 4.4, the region from which NIR photons are upscattered should be less than 0.8 AU. Dodds-Eden et al. (2009) presented first the simultaneity of X-ray and L/bands to within one sigma error bar of three minutes.

The relationship between radio and NIR/X-ray flare emission has remained unexplored due the very limited simultaneous time coverage between radio, infrared and X-ray telescopes. The continued variations of the radio flux on hourly time scale also makes the identification of radio counterparts to infrared flares difficult. In spite of this, the strong flaring in NIR/X-ray wavelengths on 2007, April 4 has given us an opportunity to examine whether there is a correlation with variability at radio frequencies. One of the key motivation of our observing campaign was to examine the adiabatic expansion picture of flaring activity of Sgr A*. One of the prediction of this model is a time delay between the peaks of optically thin NIR emission and optically thick radio emission. This implies a NIR flare with its short duration is expected to have a radio counterpart shifted in time with a longer duration. Given that there is zero time delay between NIR and X-ray light curves, as shown in Figure 23, we argue below for a radio counterpart to a strong X-ray flare by shifting and stretching the time axis of the X-ray light curve.

Figure 24a shows composite light curves of Sgr A* obtained with VLA, VLT, HST and XMM on 2007, April 4. The flux increase at 43 GHz is $\sim 40\%$ which is higher than those from the first three days of VLA observations which is $\sim 20\%$. We also know that there was no significant variation at 240 GHz during the period in which the strong NIR/X-ray flare took place. The IRAM-30m observation shows an average flux of 3.42 ± 0.26 Jy between 5 and 6h UT when the powerful NIR flare took place. The flux is mainly arising from the quiescent component of Sgr A*. Comparing the light curves of the 43 and 240 GHz data, there is no evidence for a simultaneous radio counterpart to the NIR/X-ray flare with no time delays.

We now argue that the radio flare detected between 10h and 15h UT is a time-delayed counterpart to the NIR/X-ray flare for the following reasons: i) the highest percentage of the flux increase at 43 GHz on 2007, April 4 compared to other three days of radio observations, ii) Similar morphology between radio and X-ray light curves as well the presence of three peaks in NIR and radio light curves and iii) the lack of significant flux variation above the quiescent flux of Sgr A* at 240 GHz during the NIR/X-ray flaring events. We suggest that flare emission at 43 GHz is time delayed with respect the NIR/X-ray flare emission. To explore this further, we have empirically shifted and stretched the time axis of the X-ray light curves by 5.25 hours and a factor of 3.5, respectively. The shift and stretch operation to the time axis is carried out by eye and then examined by cross correlating the time-shifted and time-stretched X-ray data and the 43 GHz light curves. The top panel of Figure 24b presents the light curve of the time-shifted and time-stretched X-ray data. The middle plot shows a baseline subtracted radio light curve. The subtraction is used to remove the contribution by the quiescent flux. We find that the best fit shows a peak in the cross correlation plot of $4.6_{-7.6}^{+9.4}$ minutes which is consistent with zero. The $1-\sigma$ error to the cross correlation peak of the shift is given in Table 2.

Given that NIR/X-ray and radio emission are expected to be optically thin and thick, respectively, the similarity in the substructures in radio and X-ray and NIR light curves and the way that they trace each other, as shown in Figure 24, are remarkable. For example, two main peaks before and after 12h UT are detected in both NIR, X-ray and radio light curves. The dips near 13:30h UT and 13h UT between radio and NIR are also seen in Figure 24a, To make a stronger case that

the X-ray/NIR and radio flares are related to each other, the morphological agreements between radio and NIR could have been improved had we used a varying time shift to different subflares or components in the NIR light curve. In fact, the shift and stretch values measured here is not unique as it is possible to decrease and increase the time-shifted and time-stretched values, respectively, and yet obtain a reasonable zero time delay between radio and X-ray data. A detailed account of these light curves in the context of adiabatic cooling plasma model will be given elsewhere.

Given that there is continuous coverage for about ten hours between 5h-15h UT in X-ray, NIR and radio wavelengths using XMM, VLT, HST, IRAM and VLA with an exception of a two-hour gap between 7 and 9h UT in radio wavelengths and a 2.5-hour gap between 10.5h and 13h UT in NIR wavelengths, we believe the lack of association between flaring activity in NIR and radio wavelengths is highly contrived. Obviously, we can not prove conclusively that radio flare seen on April 4, 2007 is associated with the NIR/X-ray flare because of two gaps in our coverage. Nevertheless, the comparison of the 43 GHz light curve with the NIR data suggest that these variations are tied closely with each other.

5.2.2. Other Cross Correlations

There were no simultaneous observations that were taken with the same instrument except with the VLA and NMA but with a small frequency separation. In spite of the small separation between the observed frequencies at 134 GHz (2.23 mm) and 146 GHz (2.05 mm), the data are taken simultaneously on 2007, April 4 with the NMA. The cross correlation of the light curves at these frequencies, as shown in Figure 25, peaks with $6_{-4.8}^{+6.6}$ minutes time delay.

Due to the limited UT coverage with individual telescopes as well as the lack of strong flaring event in this campaign (with the exception of the strong NIR/X-ray flare on 2007, April 4), the cross correlation of the light curves had difficulty following accurately the time evolution of a flare as a function of frequency. In spite of these difficulties, we have obtained cross-correlation plots of low-level fluctuations evident in four light curves. Although most of the individual cross correlation peaks have low signal-to-noise, the peaks of optically thick emission all show a tendency to lag rather lead, thus, consistent with the adiabatic expansion picture of flare emission. We have selected the best light curves to show the time lag but in fact almost all light curves systematically showed a time lag rather than a lead in their cross correlation peaks, though low signal to noise ratios. We believe the data presented here supports the plausibility of the time delay, as has also been shown in earlier cross-correlation measurements. We give four examples that indicate higher probability that the peak flare emission at high frequencies leads those at low frequencies.

Figure 26a presents the cross-correlation plot of the light curves taken at $450\mu\text{m}$ using the CSO and 230 GHz using the combined data taken from the SMA and SMT on 2007 April 3. The cross-correlation plot at the bottom of the panel shows a maximum likelihood time delay at $1.32_{-0.69}^{+1.66}$ hours. Another example shows the evidence for a time delay between 1.2mm (230 GHz) and $450\mu\text{m}$ wavelength bands on 2007, April 1 and the cross correlation plot is displayed in Figure 26b. The cross-correlation peak between these wavelength bands is $0.24_{-0.04}^{+1.48}$ hours time delay.

The cross-correlation peak between $1.70\mu\text{m}$ and 1.3mm wavelengths on 2007, April 5 is shown in Figure 26c and gives a time delay 2.64 hours with a 2σ uncertainty range of -1.66 to 3.3 hours. The NIR data for this plot combined the $1.70\mu\text{m}$ data of HST (flare 5A of Fig. 3) and the $3.8\mu\text{m}$ VLT data (flare 6 in Dodds-Eden et al. 2009). Because the spectral index of the HST data is

determined, we assumed that the preceding flare detected by the VLT at $3.8\mu\text{m}$ has the same spectral index and its duration is continuous with the brightest HST flare emission seen in this campaign. Lastly, Figure 26d shows the light curves taken with CARMA and VLA on 2007 April 02 at frequencies of 94 GHz and 43 GHz respectively. The cross correlation plot shows the strongest peak with a time delay of $1.02_{-0.31}^{+0.16}$ hours. Given that there are three peaks shown in the cross correlation plot, there is ambiguity in the determination of the true time delay from the comparison of the peaks alone. However, when the cross correlation is considered in the context of many other cross correlations plots showing similar delays of peak emission at long wavelengths following those at short wavelengths, it is clear that the primary peak signifies most likely the real time delay.

As discussed before, the strongest NIR/X-ray flare was detected on 2007, April 4 showing a peak at 5.9h UT with a full duration of about two hours in NIR wavelengths. The 2.1mm (140 GHz) light curve taken with IRAM during this period of flaring activity placed a constraint by showing a lack of flux variation with a one-sigma error of 0.26 Jy at millimetre wavelength during a strong flaring activity.

5.3. Adiabatic Expansion of Hot Plasma vs. Hot Spot Model

We discuss two models that attempt to explain the nature of the flare emission. One is an expanding hot plasma model in which the peak frequency of emission (e.g., the initial optically thin NIR flare) shifts toward lower frequencies (submillimeter, millimeter and then radio) as a self-absorbed synchrotron source cools adiabatically away from the acceleration site (Shklovskii 1960; van der Laan 1966; Yusef-Zadeh et al. 2006b, 2008). A variation of this model is a jet model in which the expansion speed of the plasma is relativistic and is collimated in the form of outflow. In the expanding blob model, polarized flare emission does not follow classical Faraday rotation and a frequency-dependent rotation measure (RM) is predicted (Yusef-Zadeh et al. 2007). The expanding blob picture considers hot plasma being launched from the disk. The cooling plasma is dominated by the magnetic pressure as the plasma escapes or remains bound to the system. The second model assumes that flares are hotspots that are orbiting within few R_s of the black hole (Broderick & Loeb 2006) where Doppler boosting and GR effects become important. The hot spot picture requires the hot plasma be embedded within the disk where the emission is dominated by the gas pressure in the disk before the hot spot plunges into the hole. Quasi-periodic flaring events are expected under the assumption that hot spots survive longer than the period of the last stable orbit. There are several issues that the hot spot model appears to be inconsistent with observations. One is the time delay between the peaks of flare emission which is not expected in this picture. It is possible that the optically thin and thick flare emission is not related to each other and that the hot spot model is applicable only to the NIR flare emission. However, recent measurements as well as measurements presented in this campaign indicate time delay between the peaks of NIR/X-ray and submillimeter flare emission (Yusef-Zadeh et al. 2008; Marrone et al. 2008; Eckart et al. 2009).

Another difficulty with the hot spot model is the lack of evidence for power on the quasi-periodicity in NIR light curve (Do et al. 2008, Meyer et al. 2008). Claims of quasi-periodic variations in the NIR lightcurves were the motivating observation for the hotspot model, but the most thorough analysis of NIR lightcurve variability have not shown evidence for significant quasi-periodic power (Do et al. 2008; Meyer et al. 2008). Furthermore, MHD simulations of accreting gas indicate that hot spots can last less than an orbital time scale before they disperse (Hawley & Balbus 2002).

A major motivation for the observational study of Sgr A* in the 2007 observing campaign was to

test predictions of the plasmon model of flare emission such as the time delay between the peak emission at different wavelengths. Previous observing campaigns to monitor Sgr A* have found evidence for time delay between the peak emission at 43 and 22 GHz. (Yusef-Zadeh et al. 2006b; Yusef-Zadeh et al. 2007a). These measurements were consistent with the predicted time delays in the plasmon model. As described above, we carried out the cross correlation of the peak of radio flare emission and the emission at other wavelength bands using simultaneous space- and ground-based observatories. These measurements would allow us to determine if radio flares are correlated with flaring in the near-IR, X-ray and sub-millimeter. The data presented here show an increasing chance of high frequency flare emission leading the low frequency emission when simultaneous data between 43 GHz, 94 GHz, 230GHz, 0.45mm and $1.70\mu\text{m}$ are examined. It is only the collection of the cross correlation plots that make the time delay between the peaks of flare emission compelling.

Another intriguing example that could be used against the orbiting hot spot model is the relationship between radio and NIR/X-ray flare emission. The light curve at 43 GHz using the VLA began covering the flare 4.5 hours after the start of the NIR flare on 2007 April 4. The morphology of the peaks in the two light curves appears to show a rise of flux followed by flattening of the emission. Figure 24b shows the comparison of the X-ray and radio light curves by shifting the X-ray light curve by about 5.25 hours and stretching by a factor of 3.5. We suggested that shifting and stretching of the light curves serve as the time delay and duration of flare as it evolves in time. The stretching of the NIR light curve by a factor of 3.5 can be viewed in the context of the expanding blob model of an initial flare or a compact blob observed in NIR followed by the expansion of a blob of hot plasma emitting in radio wavelengths. Individual NIR and radio flares show typical durations of ~ 20 min and 1-2 hours, respectively. The ratio of the observed durations is similar to the stretching factor that was applied to the time axis of the NIR light curve of flare emission. A more detailed account of this analysis in the context of the plasmon model will be given elsewhere.

Recently, Marrone et al. (2008) criticized the expanding blob model on the grounds that their measured ratio of 1.3 mm to $850\mu\text{m}$ flux during a flare on 2006 July 17 was higher than expected from the blob model, both in the optically thick precursors (where one would expect a spectral index of $5/2$ rather than the measured value $\beta = 0.1 \pm 0.5$), and in the ratio of the amplitudes of the flares at the two wavelengths. However, the continual variability at radio and millimetre means that there is a large uncertainty in determining the underlying background flux level for a particular flare, and we have determined that there are reasonable choices of the levels that renders flare profiles that are consistent with the plasmon framework. Fig. 27 demonstrates simultaneous fit to both the 1.3 mm and $850\mu\text{m}$ flux of the 2006 July 17 flares (see Figure 3 of Marrone et al. 2008) using the plasmon model. The parameters of the successful fits to the first flare peaking near 5.7 hr UT are $p = 1$, $R_0 = 0.52 R_s$, $v = 0.011c$, and $B = 73 G$ whereas the parameters of the strong flare peaking near 7.5 hr UT are $p = 0.5$, $R_0 = 0.42 R_s$, $v = 0.003c$, and $B = 75 G$. These fits show clear evidence that a simple picture of plasmon model can easily be applied to previously published light curves in submillimeter wavelengths (see additional fits to light curves in Yusef-Zadeh et al. 2008).

The other criticism of Marrone et al. (2008) is that the model requires adiabatic expansion of the blobs at speeds $\sim 0.03c$ much below than the canonical sound speed $c/\sqrt{3}$ approaching the black hole that would be expected were the blobs filled with plasma and sitting in vacuum. Given that the blob diameters are in the range of several R_s they may well be located at 10 or more R_s , where the local sound speed would be $\sim 0.1c$. In any case, they may be embedded in the outer layers of an accretion flow where they would be only mildly overpressured with respect to their surroundings

and the expansion time scale would be comparable to the buoyancy or orbital time scale.

5.4. Distribution of Electrons in the Flares

Previously we have modeled the time delays at submillimeter to radio frequencies in the expanding hot plasma model assuming that the accelerated particles have a power-law energy distribution. This is motivated by the long time scale of the flares compared to the synchrotron loss time for the expected magnetic field strengths of 10–30 G. These models assume a homogeneous sphere threaded by a uniform magnetic field. As the region expands, the relativistic particles cool by adiabatic expansion with $E \propto 1/R$ and the magnetic field is diluted as $B \propto R^{-2}$ because of flux freezing. Assuming that the relativistic electron energies run between 1 MeV and 100 MeV and that they are in equipartition with the magnetic field, the models are characterized by the particle spectral index, p (with $n(E) \propto E^{-p}$), the expansion speed v (assumed constant), and the timing and amplitude of the flaring at a single frequency. From this we can infer a magnetic field strength B and the size of the emitting region at t_0 , R_0 . Figure 28a shows an approximate fit to the CARMA and VLA data obtained on 2007 April 02 using two flares. The derived parameters of the first flare at 10.9 h UT are $p = 0.5$, $R_0 = 3.6 R_s$, $v = 0.070c$, and $B = 15 G$, while the later flare at 14.7 hr UT has $p = 1.5$, $R_0 = 9.8 R_s$, $v = 0.065c$, and $B = 13 G$. These numbers should be regarded as illustrative given the rough fitting, the simplicity of the model, and the freedom in choosing the baselines at each frequency.

While a power-law electron spectrum is plausible, the inferred spectra are significantly harder than the E^{-2} expected on the basis of the simplest version of diffusive shock acceleration. This suggests that the derived power law may instead be the effective power-law of the particle energy spectrum over the small (5%) range of initial energies relevant to our observing frequencies at 96 GHz to 43 GHz. Other spectral forms are easily introduced within the context of this model. By way of example, in Fig. 28b we show the “best” relativistic Maxwellian model, with the particle spectrum characterized by the electron temperature T_e at time t_0 instead of p . The parameters in this case ($kT_e = 0.25$ keV, $R_0 = 4.4 R_s$, $v = 0.077c$, and $B = 10 G$; $kT_e = 4.1$ MeV, $R_0 = 10.4 R_s$, $v = 0.091c$, $B = 12 G$) yields similar emission region characteristics but is worse in matching the 43 GHz data. This is because the synchrotron spectrum is more strongly peaked than for a power-law electron population. As a result, the flare amplitude declines more rapidly at successively lower frequencies than is the case for power-law models (except for large choice of p). Future simultaneous light curves with better time coverage are needed to confirm this results.

6. Conclusions

The main results of extensive observing campaign that took place in 2007 can be summarized as follows:

Simultaneous VLA and VLBA observations indicate that flare emission from Sgr A* at 43 GHz arises from within the scattering size of Sgr A* which is $\sim 0.3 \times 0.7$ mas (Bower et al. 2004) or within the inner $30 \times 70 R_s$ of Sgr A*.

We show the evidence of varying spectral index values when weak and bright NIR flares are compared. In addition, the NIR flare statistics indicate that the probability of flare emission

is proportional to the inverse of the flux density. Simulations of the histogram of such flares assuming uniform distribution of peak flare emission is consistent with observations. The significance of the probability of flare emission is inversely proportional to the flux of flare is not understood.

In addition to a powerful X-ray flare with a NIR counterpart and $11.8\mu\text{m}$ upper limit on 2007 April 4 that had been reported earlier by Porquet et al. (2008), Dodds-Edden et al. (2009), and Trap et al. (2009), we show evidence of three new X-ray flares with NIR counterparts. The origin of X-ray production is explained in the context of ICS employing the structure details of the Sgr A* emitting region inferred from intrinsic size measurements. In this picture, the seed photons associated with flares in NIR wavelengths are upscattered by the sea of electrons that are responsible for the quiescent emission of the Sgr A* in radio and submillimeter wavelengths. A prediction of this model is a time delay between the peaks of X-ray and NIR flare emission.

The comparison of the light curves at multiple wavelengths indicated time delays implying optically thick emission. We also argue a tantalizing radio flare three hours after the strongest NIR and X-ray flare detected on 2007 April 4. These measurements are consistent with an adiabatic expansion of hot plasma. Although these measurements weaken the hot spot model of flare emission, we can not distinguish whether there is jet activity associated with the observed time delays or the expansion of hot plasma that is bound to Sgr A*.

Acknowledgments:

This work is partially supported by the grant AST-0807400 from the National Science Foundation. Some of the data presented here were obtained from Mauna Kea observatories. We are grateful to the Hawai'ian people for permitting us to study the universe from this sacred summit. Research at the Caltech Submillimeter Observatory is supported by grant AST-0540882 from the National Science Foundation. Research grants are also given by Australian Research Council (DPO986386) and Macquarie University. The SMT is operated by the Arizona Radio Observatory (ARO), Steward Observatory, University of Arizona. The XMM-Newton project is an ESA Science Mission with instruments and contributions directly funded by ESA Member State and the USA (NASA).

REFERENCES

- Alexander, T. 1997, MNRAS, 285, 891
- Baars, J. W. M., Genzel, R., Pauliny-Toth, I. I. K., & Witzel, A. 1977, A&A, 61, 99
- Baars, J. W. M., Martin, R. N., Mangum, J. G., McMullin, J. P., & Peters, W. L. 1999, PASP, 111, 627
- Baganoff, F. K. 2003, in Bulletin of the American Astronomical Society, Vol. 35, Bulletin of the American Astronomical Society, 606
- Baganoff, F. K., Maeda, Y., Morris, M., Bautz, M. W., Brandt, W. N., Cui, W., Doty, J. P., Feigelson, E. D., Garmire, G. P., Pravdo, S. H., Ricker, G. R., & Townsley, L. K. 2003, ApJ, 591, 891
- Balick, B., & Brown, R. L. 1974, ApJ, 194, 265

- Bélanger, G., Goldwurm, A., Melia, F., Ferrando, P., Grosso, N., Porquet, D., Warwick, R., & Yusef-Zadeh, F. 2005, *ApJ*, 635, 1095
- Bittner, J. M., Liu, S., Fryer, C. L., & Petrosian, V. 2007, *ApJ*, 661, 863
- Blandford, R. D., & Begelman, M. C. 1999, *MNRAS*, 303, L1
- Blundell, R. 2004, in *Proceedings of the 15th International Symposium on Space Terahertz Technology*, April 27-29, 2004, p. 3, 3
- Bower, G. C., Falcke, H., Herrnstein, R. M., Zhao, J.-H., Goss, W. M., & Backer, D. C. 2004, *Science*, 304, 704
- Broderick, A. E., & Loeb, A. 2006, *ApJ*, 636, L109
- Do, T., Ghez, A. M., Morris, M. R., Yelda, S., Lu, J. R., Hornstein, S. D., & Matthews, K. 2008, *Journal of Physics Conference Series*, 131, 012003
- Dodds-Eden, K., Porquet, D., Trap, G., Quataert, E., Haubois, X., Gillessen, S., Grosso, N., Pantin, E., Falcke, H., Rouan, D., Genzel, R., Hasinger, G., Goldwurm, A., Yusef-Zadeh, F., Clenet, Y., Trippe, S., Lagage, P.-O., Bartko, H., Eisenhauer, F., Ott, T., Paumard, T., Perrin, G., Yuan, F., Fritz, T. K., & Mascetti, L. 2009, *ApJ*, 698, 676
- Doeleman, S. S., Weintroub, J., Rogers, A. E. E., Plambeck, R., Freund, R., Tilanus, R. P. J., Friberg, P., Ziurys, L. M., Moran, J. M., Corey, B., Young, K. H., Smythe, D. L., Titus, M., Marrone, D. P., Cappallo, R. J., Bock, D. C.-J., Bower, G. C., Chamberlin, R., Davis, G. R., Krichbaum, T. P., Lamb, J., Maness, H., Niell, A. E., Roy, A., Strittmatter, P., Werthimer, D., Whitney, A. R., & Woody, D. 2008, *Nature*, 455, 78
- Eckart, A., Baganoff, F. K., Morris, M., Bautz, M. W., Brandt, W. N., Garmire, G. P., Genzel, R., Ott, T., Ricker, G. R., Straubmeier, C., Viehmann, T., Schödel, R., Bower, G. C., & Goldston, J. E. 2004, *A&A*, 427, 1
- Eckart, A., Baganoff, F. K., Morris, M. R., Kunneriath, D., Zamaninasab, M., Witzel, G., Schödel, R., Garc´ıa-Mar´ın, M., Meyer, L., Bower, G. C., Marrone, D., Bautz, M. W., Brandt, W. N., Garmire, G. P., Ricker, G. R., Straubmeier, C., Roberts, D. A., Muzic, K., Mauerhan, J., & Zensus, A. 2009, *ArXiv e-prints*
- Eckart, A., Baganoff, F. K., Schödel, R., Morris, M., Genzel, R., Bower, G. C., Marrone, D., Moran, J. M., Viehmann, T., Bautz, M. W., Brandt, W. N., Garmire, G. P., Ott, T., Trippe, S., Ricker, G. R., Straubmeier, C., Roberts, D. A., Yusef-Zadeh, F., Zhao, J. H., & Rao, R. 2006a, *A&A*, 450, 535
- Eckart, A., Schödel, R., Garc´ıa-Mar´ın, M., Witzel, G., Weiss, A., Baganoff, F. K., Morris, M. R., Bertram, T., Dovciak, M., Duschl, W. J., Karas, V., König, S., Krichbaum, T. P., Krips, M., Kunneriath, D., Lu, R.-S., Markoff, S., Mauerhan, J., Meyer, L., Moutaka, J., MuVzić, K., Najarro, F., Pott, J.-U., Schuster, K. F., Sjouwerman, L. O., Straubmeier, C., Thum, C., Vogel, S. N., Wiesemeyer, H., Zamaninasab, M., & Zensus, J. A. 2008, *A&A*, 492, 337
- Eckart, A., Schödel, R., Meyer, L., Trippe, S., Ott, T., & Genzel, R. 2006b, *A&A*, 455, 1
- Edelson, R. A., & Krolik, J. H. 1988, *ApJ*, 333, 646

- Eisenhauer, F., Genzel, R., Alexander, T., Abuter, R., Paumard, T., Ott, T., Gilbert, A., Gillessen, S., Horrobin, M., Trippe, S., Bonnet, H., Dumas, C., Hubin, N., Kaufer, A., Kissler-Patig, M., Monnet, G., Ströbele, S., Szeifert, T., Eckart, A., Schödel, R., & Zucker, S. 2005, *ApJ*, 628, 246
- Falcke, H., Goss, W. M., Matsuo, H., Teuben, P., Zhao, J.-H., & Zylka, R. 1998, *ApJ*, 499, 731
- Falcke, H., & Markoff, S. 2000, *A&A*, 362, 113
- Falcke, H., Markoff, S., & Bower, G. C. 2009, *A&A*, 496, 77
- Genzel, R. 2000, *ArXiv Astrophysics e-prints*
- Genzel, R., Schödel, R., Ott, T., Eckart, A., Alexander, T., Lacombe, F., Rouan, D., & Aschenbach, B. 2003, *Nature*, 425, 934
- Genzel, R., & Townes, C. H. 1987, *ARA&A*, 25, 377
- Ghez, A. M., Becklin, E., Duchjne, G., Hornstein, S., Morris, M., Salim, S., & Tanner, A. 2003, *Astronomische Nachrichten Supplement*, 324, 527
- Ghez, A. M., Salim, S., Hornstein, S. D., Tanner, A., Lu, J. R., Morris, M., Becklin, E. E., & Duchêne, G. 2005, *ApJ*, 620, 744
- Ghez, A. M., Salim, S., Weinberg, N. N., Lu, J. R., Do, T., Dunn, J. K., Matthews, K., Morris, M. R., Yelda, S., Becklin, E. E., Kremenek, T., Milosavljevic, M., & Naiman, J. 2008, *ApJ*, 689, 1044
- Ghez, A. M., Wright, S. A., Matthews, K., Thompson, D., Le Mignant, D., Tanner, A., Hornstein, S. D., Morris, M., Becklin, E. E., & Soifer, B. T. 2004, *ApJ*, 601, L159
- Gillessen, S., Eisenhauer, F., Quataert, E., Genzel, R., Paumard, T., Trippe, S., Ott, T., Abuter, R., Eckart, A., Lagage, P. O., Lehnert, M. D., Tacconi, L. J., & Martins, F. 2006, *ApJ*, 640, L163
- Gillessen, S., Eisenhauer, F., Trippe, S., Alexander, T., Genzel, R., Martins, F., & Ott, T. 2009, *ApJ*, 692, 1075
- Goldston, J. E., Quataert, E., & Igumenshchev, I. V. 2005, *ApJ*, 621, 785
- Goldwurm, A., Brion, E., Goldoni, P., Ferrando, P., Daigne, F., Decourchelle, A., Warwick, R. S., & Predehl, P. 2003, *ApJ*, 584, 751
- Hawley, J. F., & Balbus, S. A. 2002, *ApJ*, 573, 738
- Hornstein, S. D., Matthews, K., Ghez, A. M., Lu, J. R., Morris, M., Becklin, E. E., Rafelski, M., & Baganoff, F. K. 2007, *ApJ*, 667, 900
- Kreysa, E. 1990, in *Liege International Astrophysical Colloquia*, Vol. 29, *Liege International Astrophysical Colloquia*, ed. B. Kaldeich, 265–270
- Li, H., Dowell, C. D., Kirby, L., Novak, G., & Vaillancourt, J. E. 2008, *Appl. Opt.*, 47, 422
- Liu, S., & Melia, F. 2001, *ApJ*, 561, L77

- . 2002, *ApJ*, 566, L77
- Liu, S., Melia, F., & Petrosian, V. 2006, *ApJ*, 636, 798
- Liu, S., Petrosian, V., & Melia, F. 2004, *ApJ*, 611, L101
- Markoff, S., Falcke, H., Yuan, F., & Biermann, P. L. 2001, *A&A*, 379, L13
- Marrone, D. P., Baganoff, F. K., Morris, M. R., Moran, J. M., Ghez, A. M., Hornstein, S. D., Dowell, C. D., Muñoz, D. J., Bautz, M. W., Ricker, G. R., Brandt, W. N., Garmire, G. P., Lu, J. R., Matthews, K., Zhao, J.-H., Rao, R., & Bower, G. C. 2008, *ApJ*, 682, 373
- Marrone, D. P., & Rao, R. 2008, in Presented at the Society of Photo-Optical Instrumentation Engineers (SPIE) Conference, Vol. 7020, Society of Photo-Optical Instrumentation Engineers (SPIE) Conference Series
- Melia, F. 1992, *ApJ*, 387, L25
- Melia, F. 2002, in Bulletin of the American Astronomical Society, Vol. 34, Bulletin of the American Astronomical Society, 951
- Meyer, L., Do, T., Ghez, A., Morris, M. R., Witzel, G., Eckart, A., Bélanger, G., & Schödel, R. 2008, *ApJ*, 688, L17
- Meyer, L., Eckart, A., Schödel, R., Duschl, W. J., Mu Vzić, K., Dov Vciak, M., & Karas, V. 2006, *A&A*, 460, 15
- Moneti, A., Stolovy, S., Blommaert, J. A. D. L., Figer, D. F., & Najarro, F. 2001, *A&A*, 366, 106
- Narayan, R., Mahadevan, R., Grindlay, J. E., Popham, R. G., & Gammie, C. 1998, *ApJ*, 492, 554
- Narayan, R., Yi, I., & Mahadevan, R. 1995, *Nature*, 374, 623
- Nayakshin, S., & Sunyaev, R. 2003, *MNRAS*, 343, L15
- Porquet, D., Grosso, N., Predehl, P., Hasinger, G., Yusef-Zadeh, F., Aschenbach, B., Trap, G., Melia, F., Warwick, R. S., Goldwurm, A., Bélanger, G., Tanaka, Y., Genzel, R., Dodds-Eden, K., Sakano, M., & Ferrando, P. 2008, *A&A*, 488, 549
- Porquet, D., Predehl, P., Aschenbach, B., Grosso, N., Goldwurm, A., Goldoni, P., Warwick, R. S., & Decourchelle, A. 2003, *A&A*, 407, L17
- Reid, M. J., & Brunthaler, A. 2004, *ApJ*, 616, 872
- Scargle, J. D. 1982, *ApJ*, 263, 835
- Schödel, R., Ott, T., Genzel, R., Hofmann, R., Lehnert, M., Eckart, A., Mouawad, N., Alexander, T., Reid, M. J., Lenzen, R., Hartung, M., Lacombe, F., Rouan, D., Gendron, E., Rousset, G., Lagrange, A.-M., Brandner, W., Ageorges, N., Lidman, C., Moorwood, A. F. M., Spyromilio, J., Hubin, N., & Menten, K. M. 2002, *Nature*, 419, 694
- Shklovskii, I. S. 1960, *Soviet Astronomy*, 4, 355

- Trap, G., Goldwurm, A., Terrier, R., Dodds-Eden, K., Gillessen, S., Genzel, R., Pautin, E., Lagage, P., Ferrando, P., Belanger, G., Porquet, D., Grosso, N., Yusef-Zadeh, F., & Melia, F. 2009, *Advances in Space Research*, submitted
- van der Laan, H. 1966, *Nature*, 211, 1131
- Yuan, F., Markoff, S., & Falcke, H. 2002, *A&A*, 383, 854
- Yuan, F., Quataert, E., & Narayan, R. 2003, *ApJ*, 598, 301
- Yusef-Zadeh, F., Bushouse, H., Dowell, C. D., Wardle, M., Roberts, D., Heinke, C., Bower, G. C., Vila-Vilaró, B., Shapiro, S., Goldwurm, A., & Bélanger, G. 2006a, *ApJ*, 644, 198
- Yusef-Zadeh, F., Roberts, D., Wardle, M., Heinke, C. O., & Bower, G. C. 2006b, *ApJ*, 650, 189
- Yusef-Zadeh, F., Wardle, M., Heinke, C., Dowell, C. D., Roberts, D., Baganoff, F. K., & Cotton, W. 2008, *ApJ*, 682, 361
- Zylka, R., Mezger, P. G., & Lesch, H. 1992, *A&A*, 261, 119

Table 1. Spectral Index Distribution Using NICMOS

Event	F(1.45 $\mu\text{m} \pm \sigma$)	F(1.70 $\mu\text{m} \pm \sigma$)	$\beta \pm \sigma$
5A	8.55 \pm 0.4	9.61 \pm 0.4	0.73 \pm 0.39
2A	6.77 \pm 0.6	7.92 \pm 0.5	0.97 \pm 0.68
2C	4.54 \pm 0.1	6.54 \pm 0.7	2.29 \pm 0.27
4A	4.77 \pm 0.1	6.14 \pm 0.3	1.59 \pm 0.33
5B	2.31 \pm 0.5	3.62 \pm 0.4	2.82 \pm 1.51
7A	2.85 \pm 0.3	3.63 \pm 0.2	1.52 \pm 0.74

Table 2. Measured Time Lags with 1- σ Errors

Date	Time Delay					
	84-43 (GHz-GHz) (hr)	134-146 (GHz-GHz) (min)	450-230 (μm -GHz) (hr)	1.70-230 (μm -GHz) (hr)	X-ray-43 (2-10keV-GHz) ^a (min)	3.8-X-rays (μm -2-10keV) (min)
2007	—	—	0.24(-0.29, +1.12)	—	—	—
April	1.02(-0.31, +0.16)	—	—	—	—	—
	—	—	1.32(-0.63, +0.33)	—	—	—
	—	3(-8.0, +3.4)	—	—	4.6(-7.6, +9.4)	0.5(-6.5, +7)
	—	—	—	2.64 (-0.67, +0.5)	—	—

^aThe X-ray data is time-shifted by 5.25 hours and time-stretched by 3.5

Observational Schedule: The April 2007 Campaign

	April 1	April 2	April 3	April 4	April 5	April 6	April 7	April 10	April 11
HST 1.7, 1.4 μ m	█	█	█	█	█	█	█		
XMM 2-12 keV	█	█	█	█					
CSO 350, 450, 850 μ m	█	█	█	█	█	█			
VLA 43, 22 GHz	█	█	█	█					
SMA 230 GHz	█		█	█	█				
CARMA 240 GHz		█	█	█	█				
IRAM 240 GHz	█	█	█	█					
NMA 90, 130 GHz	█	█	█	█					
SMT 250 GHz	█	█	█	█	█				
VLT 2.2, 3.8, 11.8 μ m,	█	█	█	█	█	█			
GMRT 0.3, 0.6, 1.3GHz		█	█	█					
INTEGRAL 20-100 keV	█	█	█	█					
VLBA 14, 22,43 GHz	█	█			█			█	█

Fig. 1.— A schematic diagram showing 13 telescopes joining the 2007 April campaign. The width of individual observing period is not scaled.

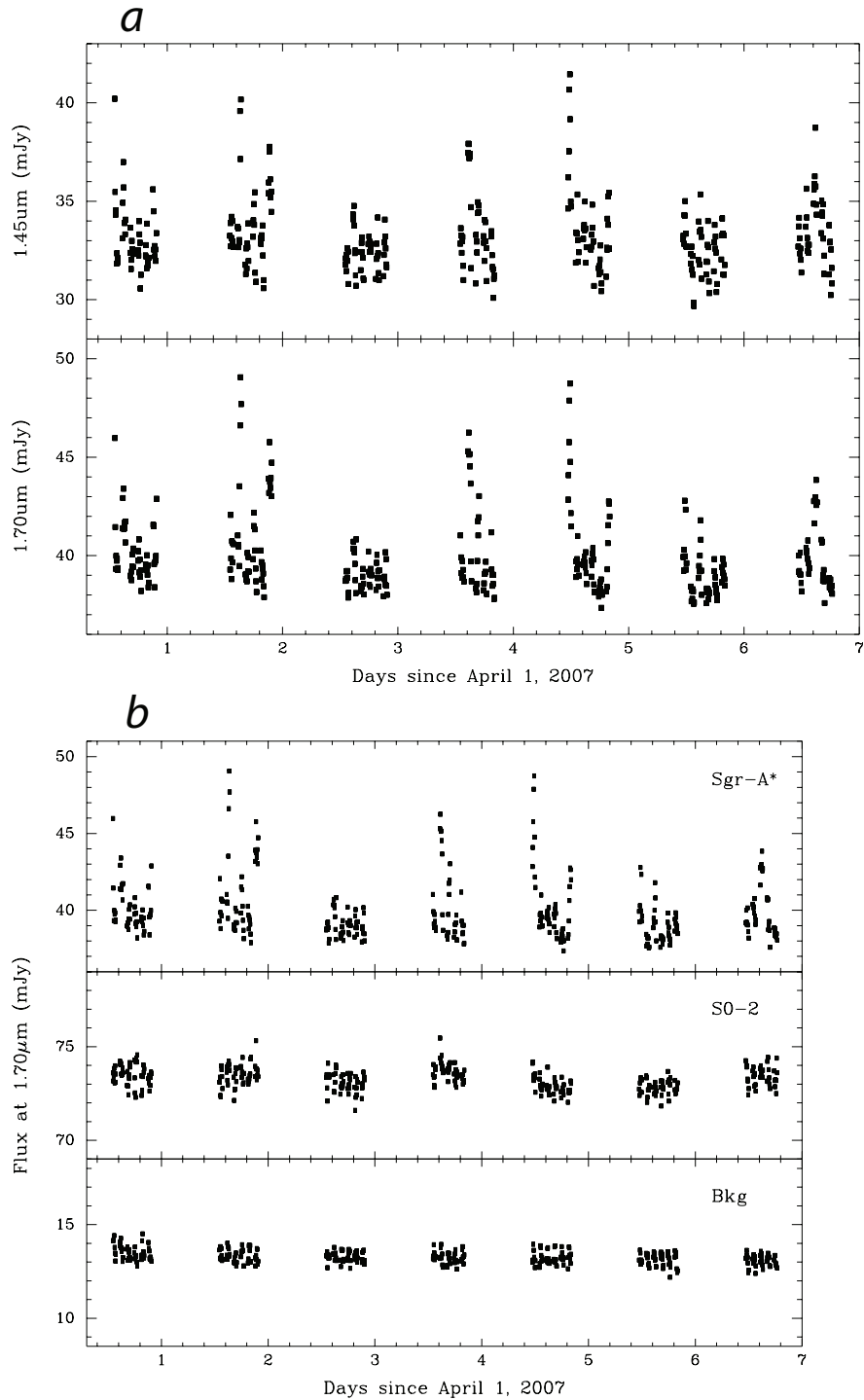


Fig. 2.—: (a) The light curves of Sgr A* at $1.45\mu\text{m}$ and $1.70\mu\text{m}$ for the seven windows of HST observations on 2007 April 1–7. No background flux is removed from these plots. (b) The HST $1.70\mu\text{m}$ light curves of Sgr A*, the star S0-2, and a region of background emission. The constancy of the S0-2 and background light curves strongly suggest that the variability of Sgr A* emission is intrinsic to Sgr A*.

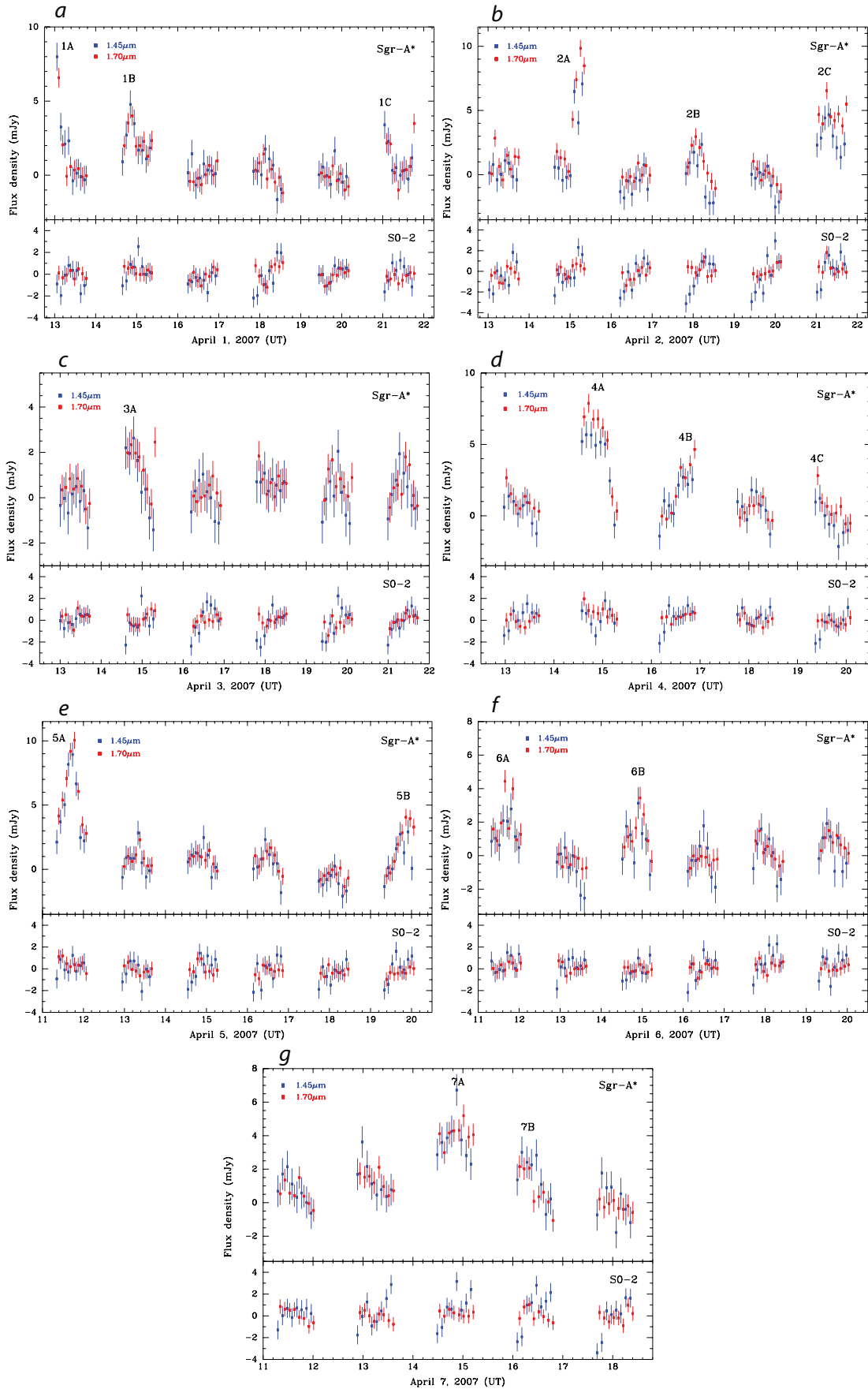


Fig. 3.— The background subtracted light curves of Sgr A* and S0-2 for each of the seven HST observing windows, with flare events labeled. The data points at 1.70 and 1.45 μm are sampled at 144 sec intervals.

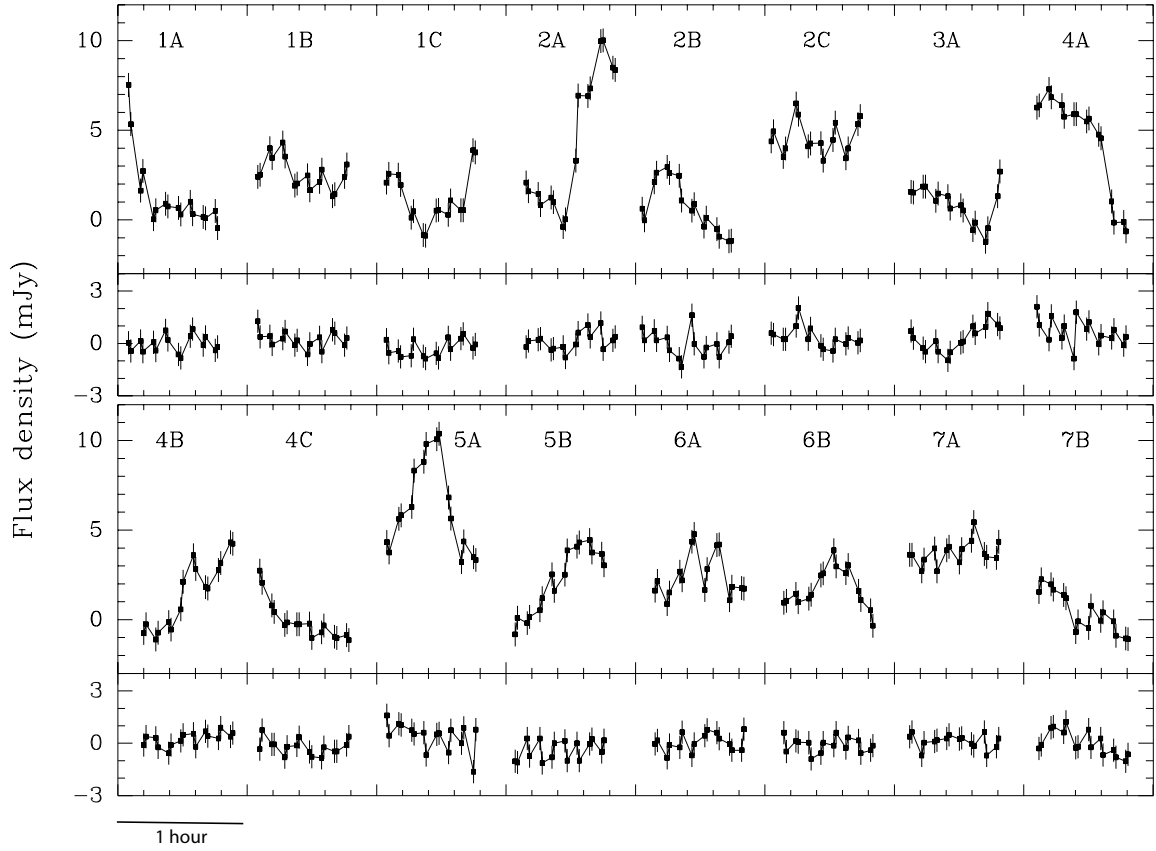


Fig. 4.— This plot shows all the 64-sec sampled data for the 16 periods that flares are identified. The 16 periods are stacked on the top and bottom panels. The x-axis is the elapsed time - each flare episode occupies a 45-minute slice within the 8-hour axis. Each flare event is labeled, as defined in Figure 3, The Sgr A* and S0-2 light curves are on the upper and lower portion of the panel. The data show only the $1.70\mu\text{m}$ photometry sampled at intervals of 64 sec but the light curves for each flare are laid side by side.

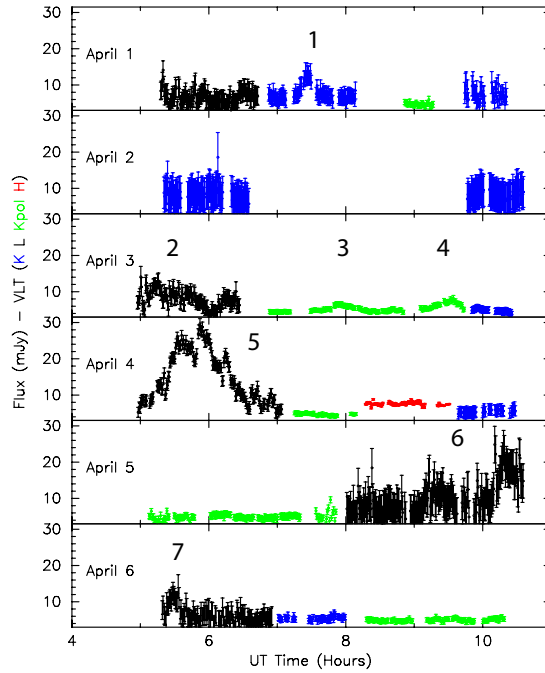


Fig. 5.—: Light curves of SgrA* for April 1-6 at H ($1.66 \mu\text{m}$), in red, K_s ($2.12\mu\text{m}$), in blue, K_s in polarimetric mode in blue and L' ($3.8\mu\text{m}$), in black, bands. are taken from Dodds-Eden et al. (2009). There are a total of seven periods of flaring activity reported in these observations. The brightest flares occurred on 2007, April 4 and April 5.

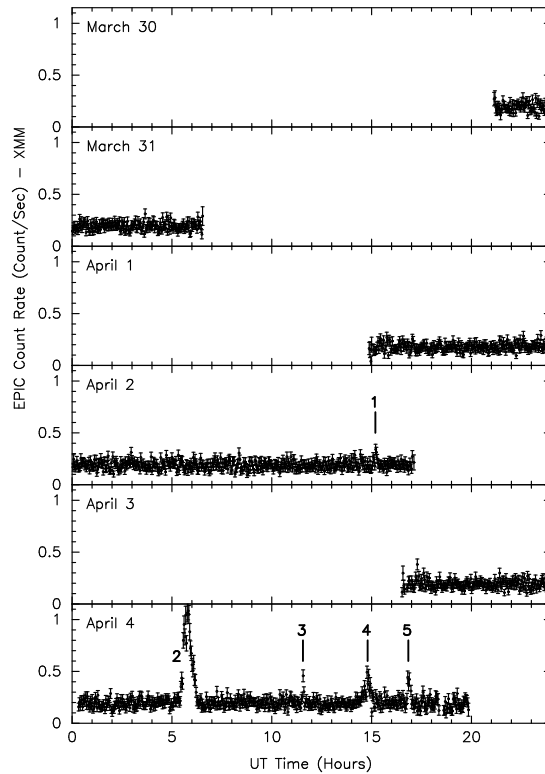


Fig. 6.—: Light curves of all the X-ray data taken with the XMM-Newton during the 2007 April observing campaign (Porquet et al. 2008). The data are averaged over a 144sec sampling. Five X-ray flares are detected, four of which had simultaneous coverage with the VLT and HST and showed NIR counterparts.

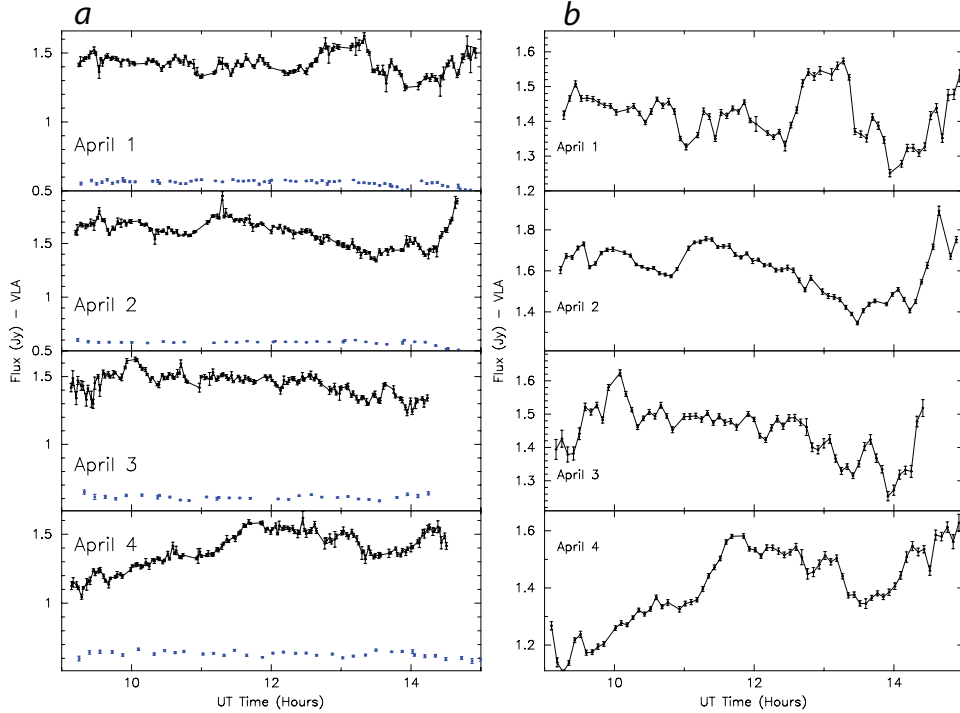


Fig. 7.—: (a - Left) Light curves of Sgr A* and the calibrator 17444-31166 at 43 GHz data obtained with VLA observations taken during 2007, April 1-4. The sampling time is 87s for Sgr A* and 90 sec for the calibrator at the bottom of each panel. The Sgr A* uv data is restricted to $>100k\lambda$ in order to suppress the contribution of extended emission. (b - Right) Similar to (a) except that only the light curves of Sgr A* are shown with a sampling time of 300 sec.

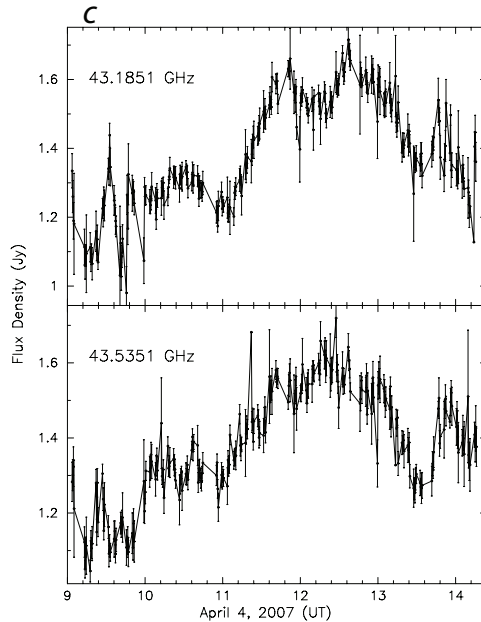


Fig. 7.—: (c) The light curves of Sgr A* on 2007, April 4 are shown in the top and bottom panels at 43.185 GHz and 43.535 GHz, respectively. The light curves are shown with a 30s sampling time. The data points with large error bars correspond to a small number of data points in a given sample. The data corresponding to minimum and maximum uv baselines are selected between 110 and 125 $k\lambda$.

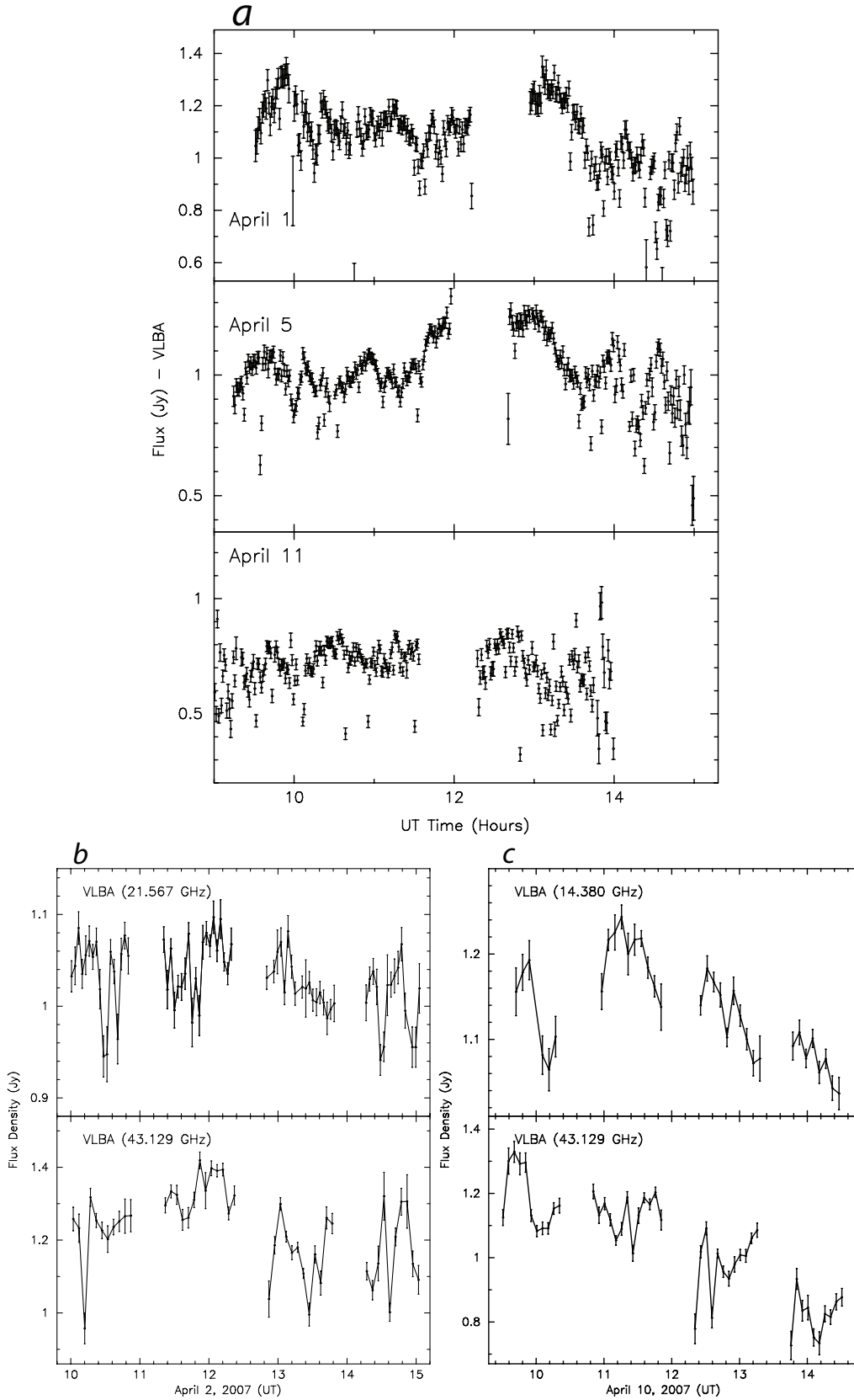


Fig. 8.— (a - Top) Light curves of Sgr A* on 2007, April 1, 5 and 11 using VLBA at 43.22 GHz. The sampling time is 60 sec. (b - Bottom Left) The light curve of Sgr A* observed with VLBA on April 2, 2007 at 22 and 43 GHz. The sampling time is 300 sec. (c - Bottom Right) The light curve of Sgr A* observed with VLBA on April 10, 2007 at 14 and 43 GHz. The sampling time is 300 sec.

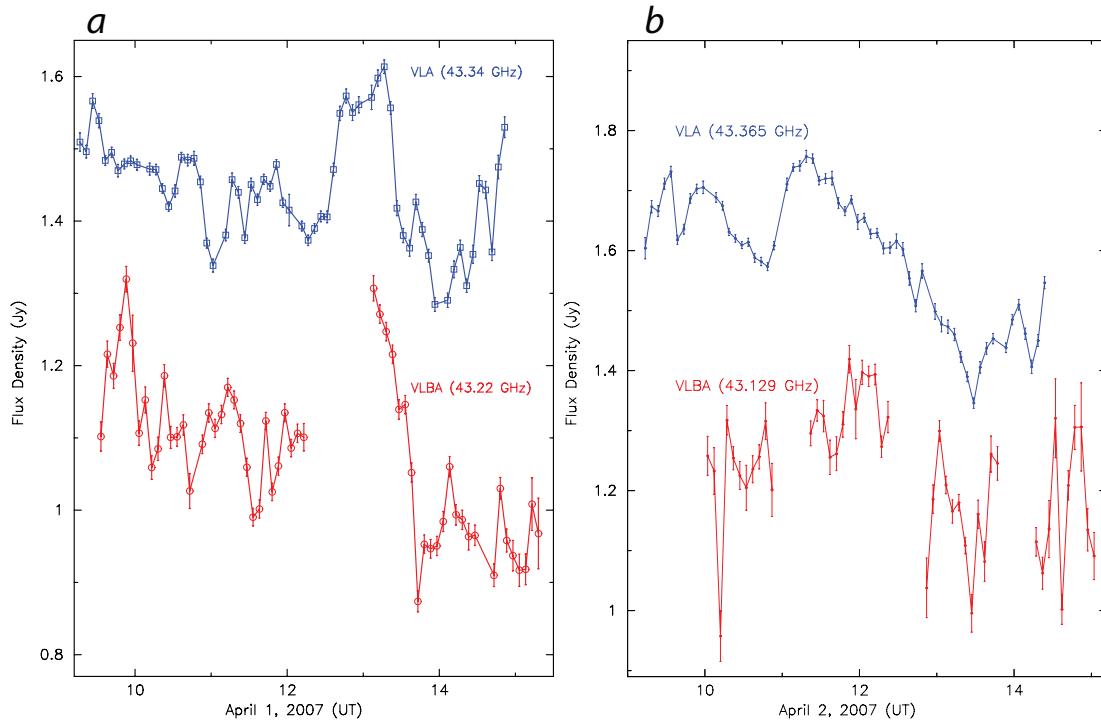


Fig. 9.—: (*a - Left*) The light curve of Sgr A* observed with VLA and VLBA on April 1, 2007. The sampling time is 300 sec. The center frequencies of the VLA and VLBA light curves correspond to 43.34 GHz 43.22 GHz, respectively. The selected VLA uv data is $>100k\lambda$. (*b - Right*) Similar to (a) except that the observations are carried out on April 2 at 43 GHz. VLBA observations on April 1 (bottom panel) are sampled continuously unlike those made on April 2. VLBA plots are shown in red (bottom) whereas VLA plots are shown in blue (top).

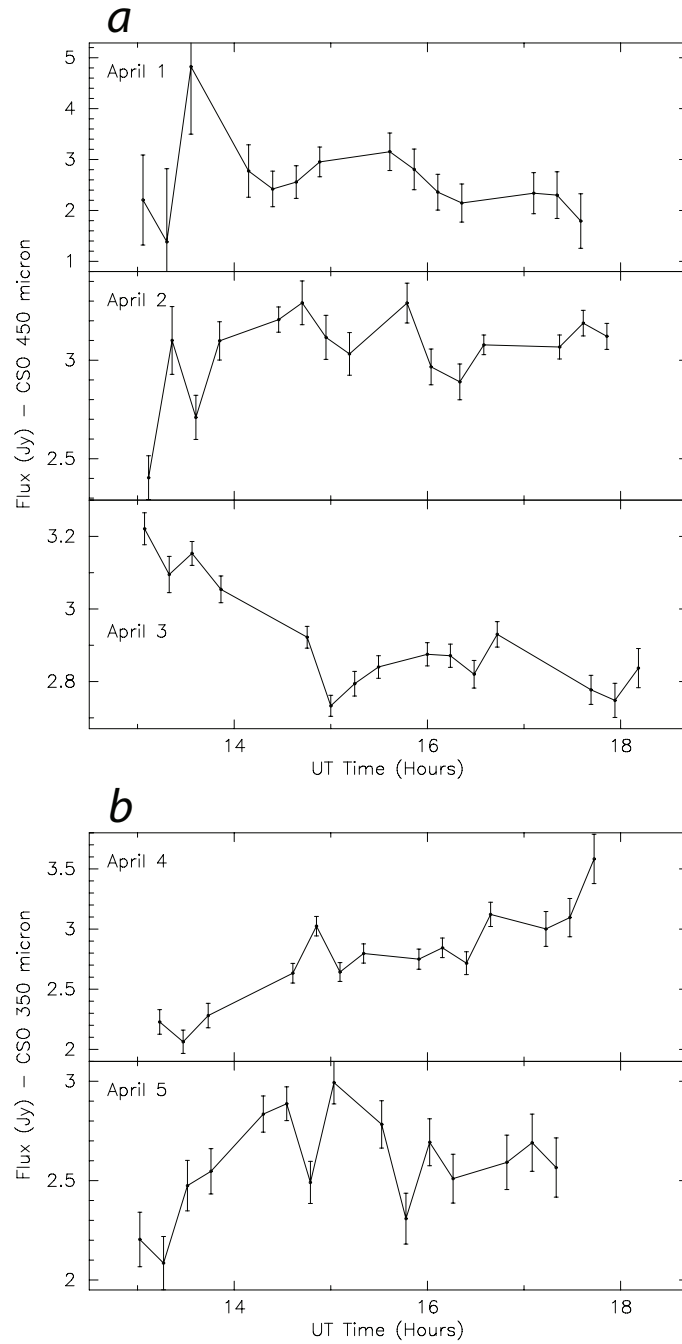


Fig. 10.—: (a) Light curves of Sgr A* at $450\mu\text{m}$ based on CSO observations on 2007, April 1-3 with a sampling time of 15 minutes. (b) Similar to (a) except at $350\mu\text{m}$ on 2007, April 4-5 with a sampling time of 15 minutes.

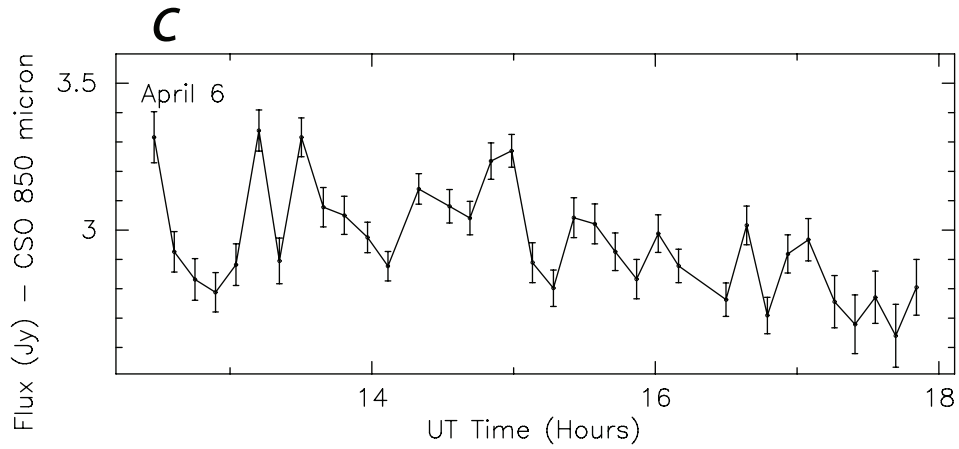


Fig. 10.—: (c) Similar to (a) except at 850 μ m on 2007, April 6 using a sampling time of 10 minutes.

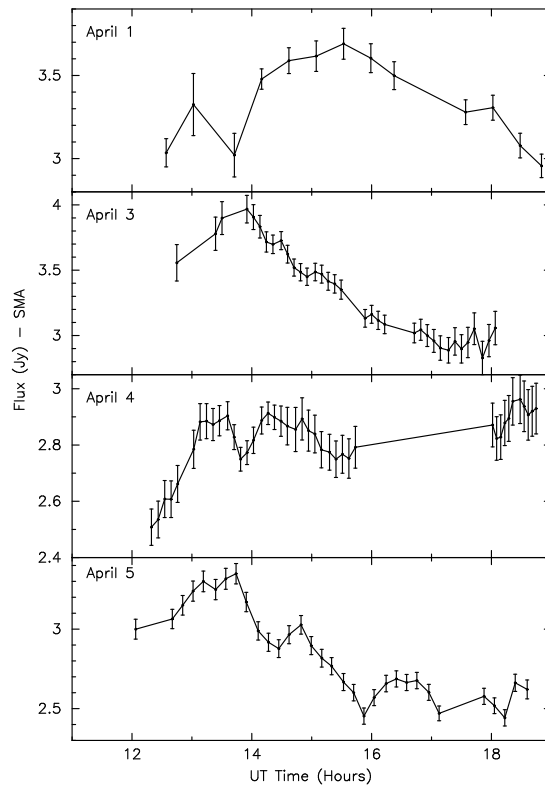


Fig. 11.—: Light curves of Sgr A* at 230 GHz using SMA on 2007 April 1, and 3-5. The sampling times are 27 min, 6.5 min, 8 min and 10 min for the April 1, 3, 4 and 5 light curves, respectively.

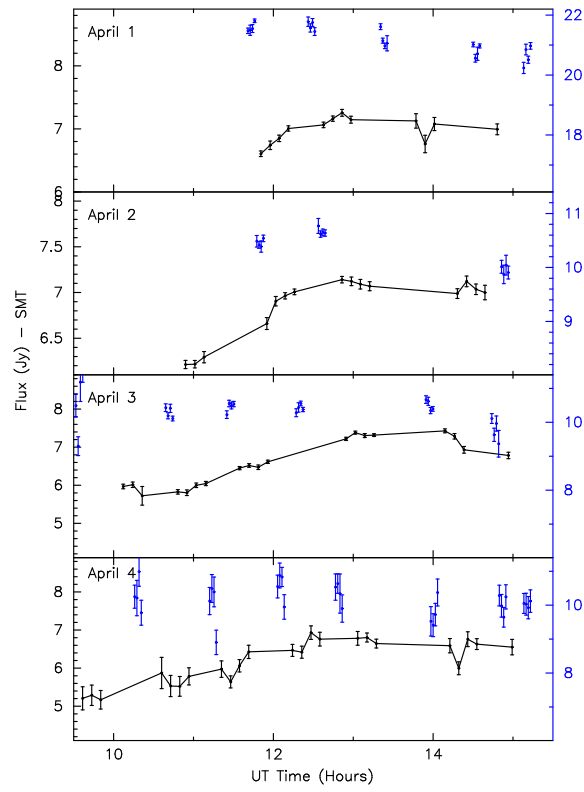


Fig. 12.—: Light curves of Sgr A* and the calibrator G34.3 and 1757-240 (blue) at 230 GHz using SMT on 2007 April 1 and April 2-4, respectively, with a sampling time of ~ 7 minutes.

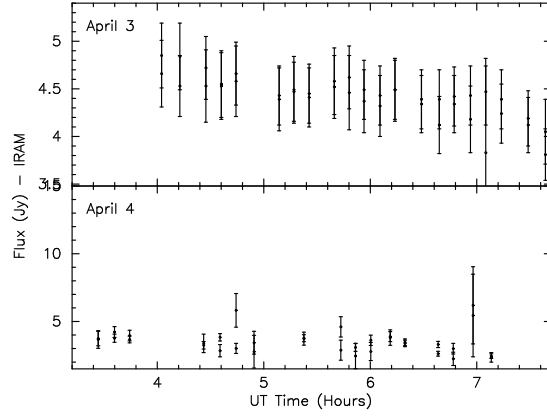


Fig. 13.—: Light curves of Sgr A* at 240 GHz (1.25mm) taken with IRAM on 2007, April 3-4 with sampling time of ~ 10 minutes. For each time sample, there are two data points estimating the flux of SgrA* from repeated pointing measurements.

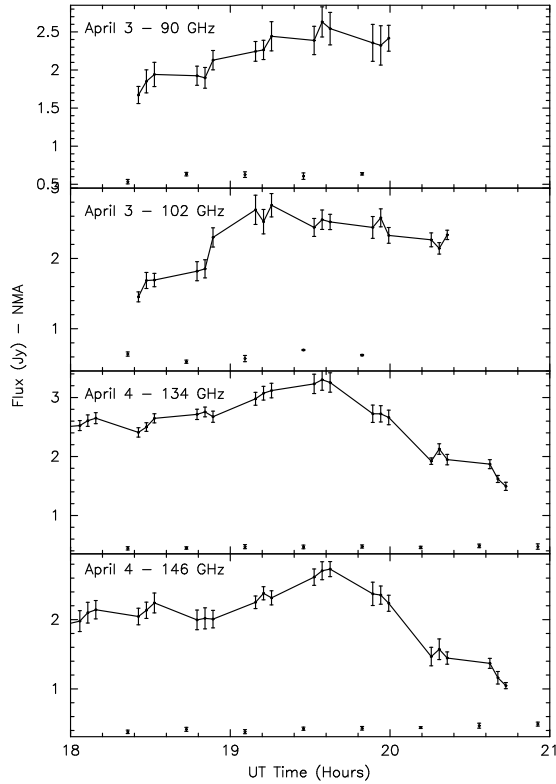


Fig. 14.—: Light curves of Sgr A* taken with the NMA. The top panels show the light curves of Sgr A* at 90 GHz and 102 GHz on April 3 whereas the bottom two panels show simultaneous light curves at 2.23mm (134 GHz) and 146 GHz on 2007, April 4. The flux of the calibrator 1744-312 is shown at the bottom of each panel. The sampling time is 3 minutes.

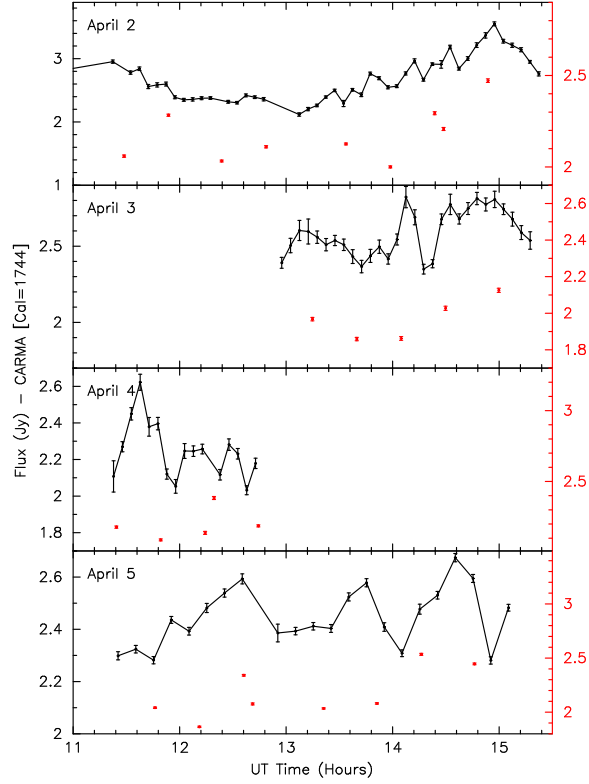


Fig. 15.—: Light curves of Sgr A* and the calibrator 1730-130 obtained with CARMA at 90 GHz with a sampling time of 300 sec on 2007, April 2-5. The uv data $> 20k\lambda$ are used to make the Sgr A* light curves.

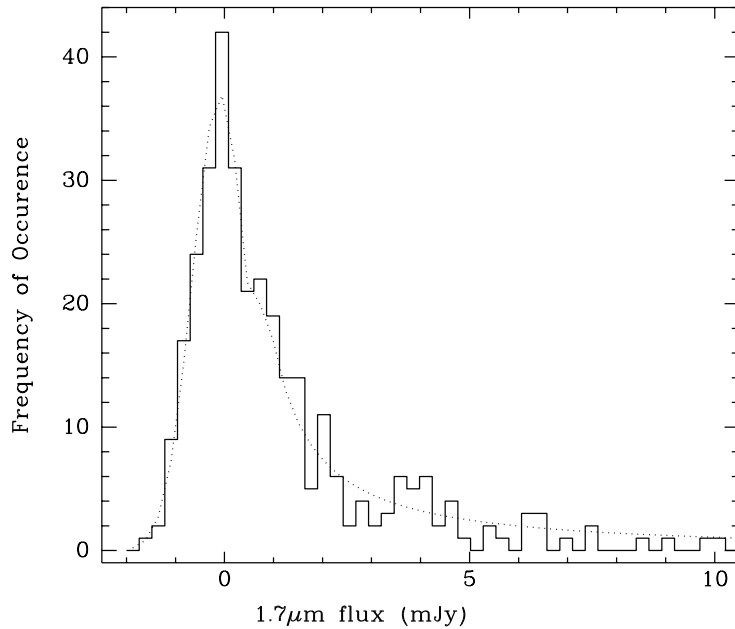


Fig. 16.—: A histogram plot of the detected signals and the noise at $1.70\mu\text{m}$ as well as the simultaneous single Gaussian fit and power law fits to both the noise and the flares. The dotted lines show the Gaussian and power law fits.

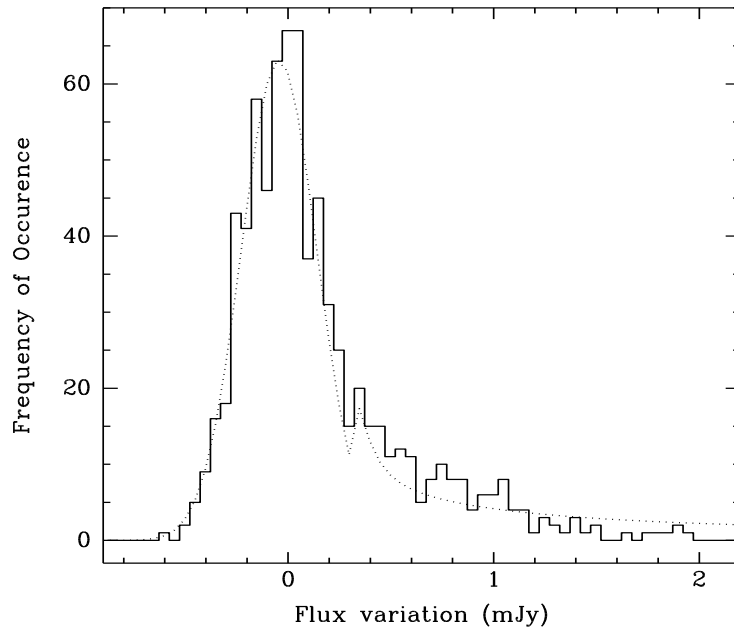


Fig. 17.—: Similar to Figure 16 expect that the 2004 histogram of flare activity (Yusef-Zadeh et al. 2006) is plotted at $1.60\mu\text{m}$.

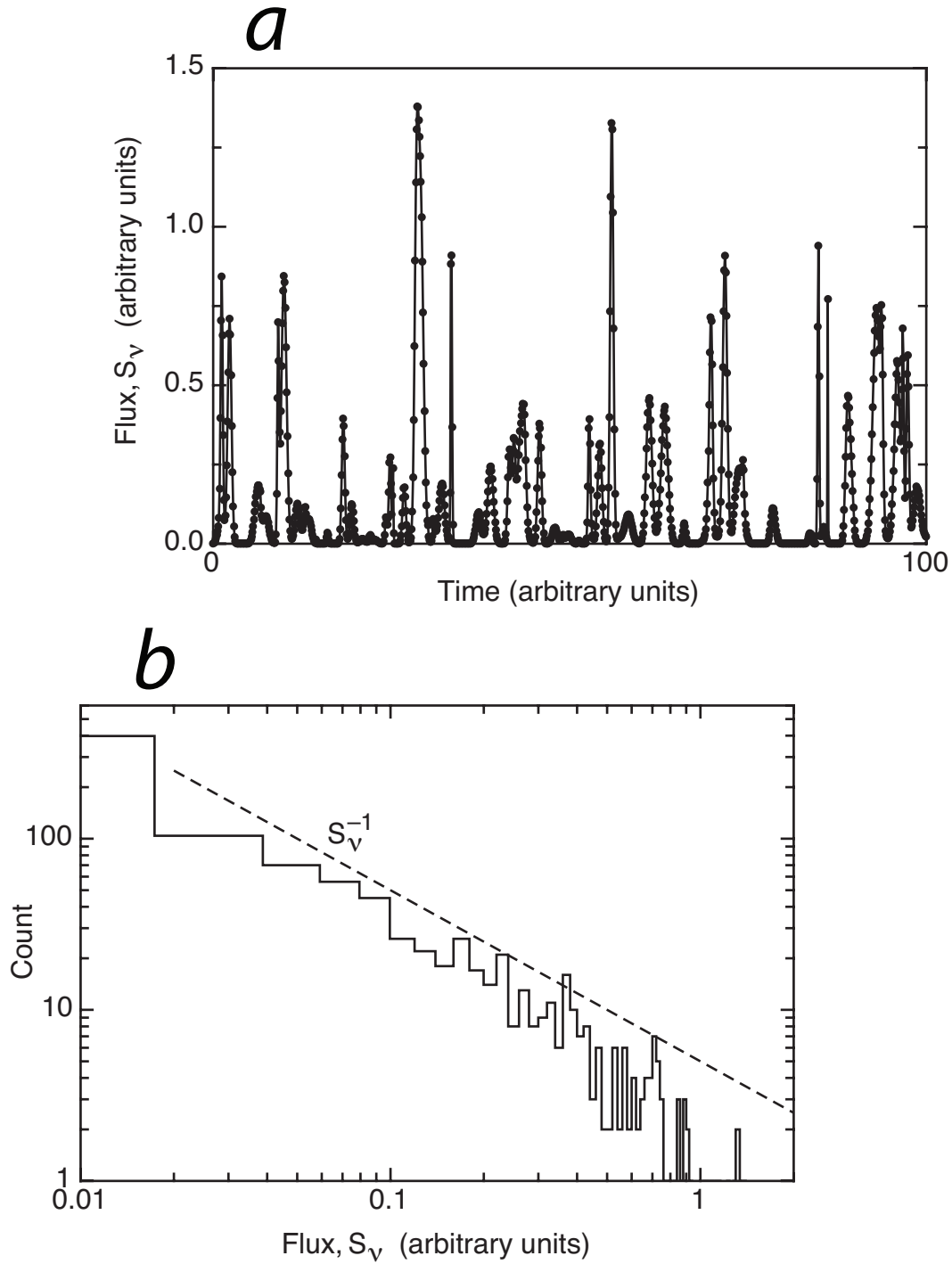


Fig. 18.—: (a) (Left) A synthetic light curve constructed from the sum of 100 Gaussian profiles with peak positions and, standard deviations drawn uniformly between -1.5 to 101.5 and 0 to 0.5 time units respectively; the probability distribution of the peak fluxes are distributed as $1/(\text{peak flux})$ between 0.01 and 1 flux units. (b) (Right) Distribution of uniformly sampled flux values in the simulated flares. The dashed line indicates a slope of $1/S_v$.

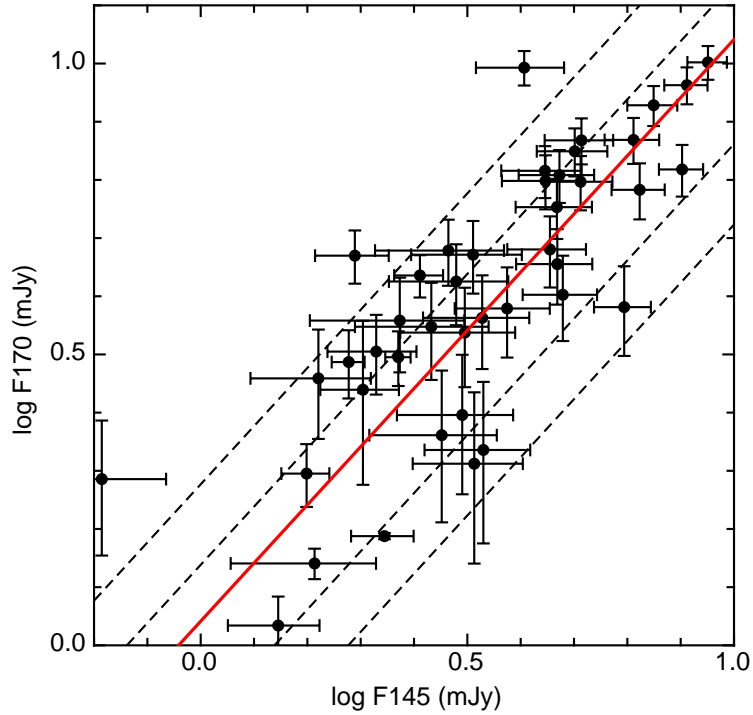


Fig. 19.—: A log-log plot of NIR fluxes in the F170 and F145 filters of NICMOS at $1.70\mu\text{m}$ and $1.45\mu\text{m}$, respectively. The thick line in red shows the spectral index $\beta=0.6$. The thin dotted lines to the right and left of the $\beta = 0.6$ line correspond to $\beta = -2, -4$ and $\beta = +2, +4$, respectively.

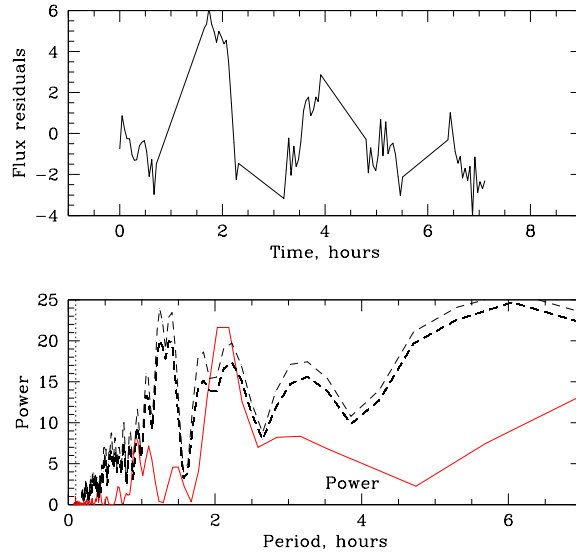


Fig. 20.—: The top and bottom boxes show the light curve of 2007, April 4 based on HST observations and the corresponding power spectrum of the residual flux of Sgr A*, respectively. The dashed lines show the significance of the power spectrum at 99% and 99.9% confidence levels. We explain the significance of the peak in the text.

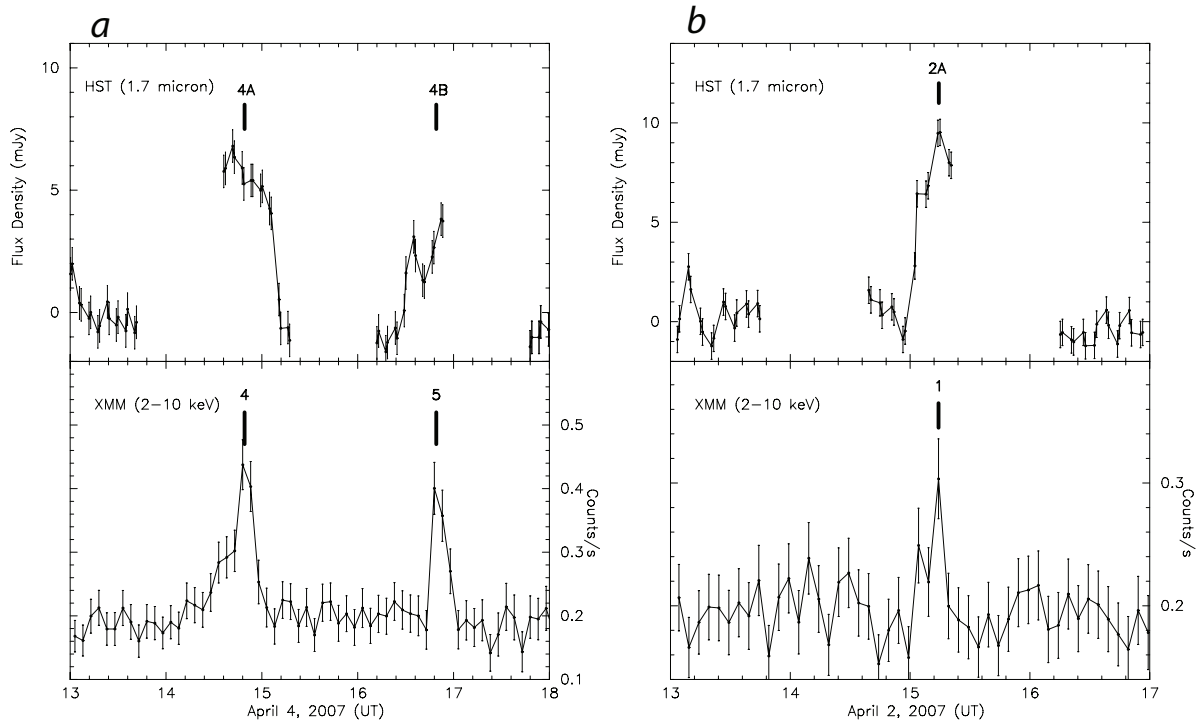


Fig. 21.—: (*a - Left*) The top panel shows the light curves of two near-IR flares identified as 4A and 4B measured with NICMOS on 2007, April 4 with a sampling time of 64s at $1.70\mu\text{m}$. The bottom panel shows the X-ray counterpart to these flares with a sampling time of 300 sec. These X-ray flares are identified as flare #4 and #5 by Porquet et al. (2008). (*b - Right*) Similar to (a) except for a NIR and X-ray flare that occurred on April 2, 2007.

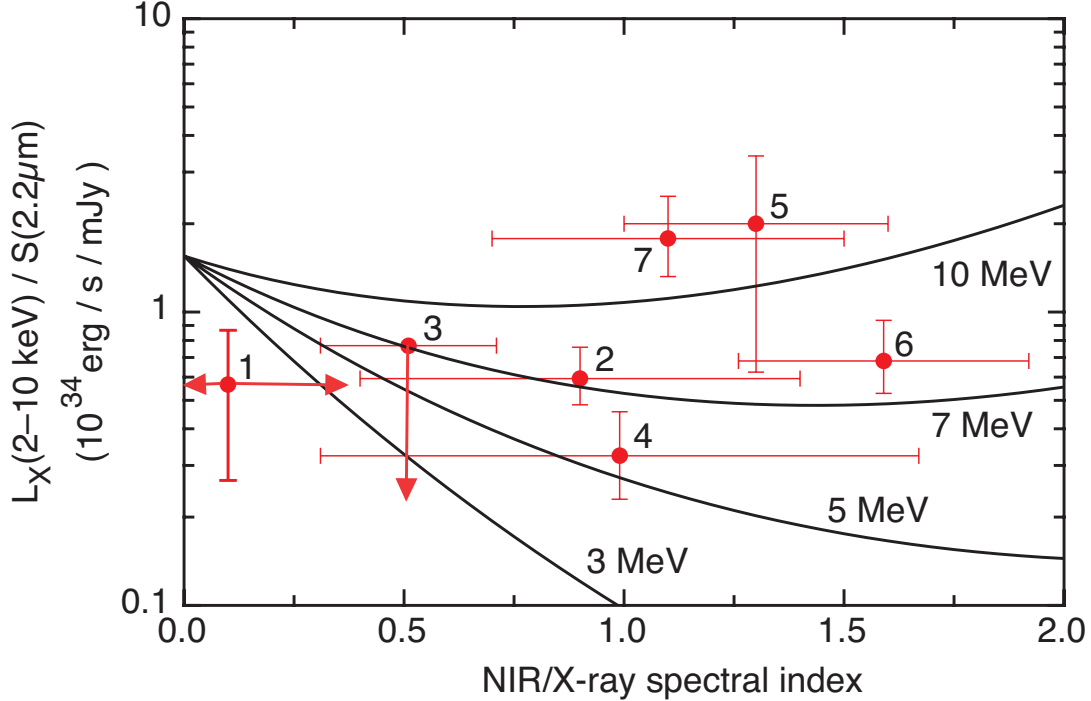


Fig. 22.—: Solid curves show the ratio of inverse Compton X-ray luminosity (2–10 keV) to NIR synchrotron flux (at $2.2\mu\text{m}$) as a function of NIR or X-ray spectral index β . Points labeled 1 to 7 indicate the measured ratios and IR spectral indices of the seven X-ray flares with known NIR counterparts. (1) 2004 July 07, Eckart et al. (2006, X-ray: flare ϕ_3 , IR: flare III); (2) 2004 Aug 31, X-ray: Belanger et al. (2005), IR: Yusef-Zadeh et al. (2006); (3) 2006 July 17, X-ray: Marrone et al. (2008), IR: lower limit from Hornstein et al. (2007); (4) 2007 April 02, X-ray: Porquet et al. (2008, flare 1), IR: this paper (flare 2A); (5) 2007 April 04 05:25, X-ray: Porquet et al. (2008, flare 2), IR: Dodds-Eden et al. (2009); (6) 2007 April 04 14:37, X-ray: Porquet et al. (2008, flare 4), IR: this paper (flare 4A); and (7) 2007 April 04 16:45, X-ray: Porquet et al. (2008, flare 5), IR: upper limit from this paper (flare 4B). Where the NIR spectral index is not known, the measured X-ray spectral index is used (points 2, 5 and 7); the NIR and X-ray spectral indices are both unknown for point 1. NIR measurements for points 2–7 are scaled to $2.2\mu\text{m}$ using either the NIR or X-ray spectral index. The measured 2–8 keV X-ray luminosities for points 1 and 3 have been rescaled to 2–10 keV by multiplication by $4/3$.

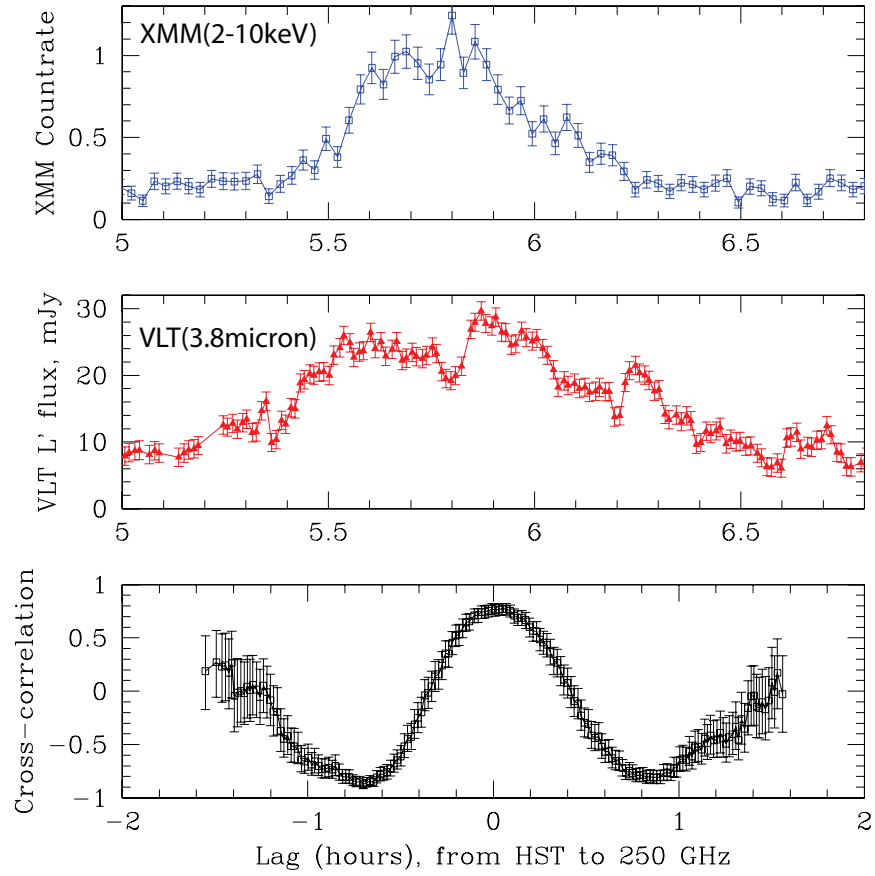


Fig. 23.—: The top and middle plots show the X-ray and NIR light curves taken on 2007, April 4. The cross correlation plot in the bottom panel indicates a peak at $-0.5^{+7.0}_{-6.5}$ minutes time delay which is consistent with zero

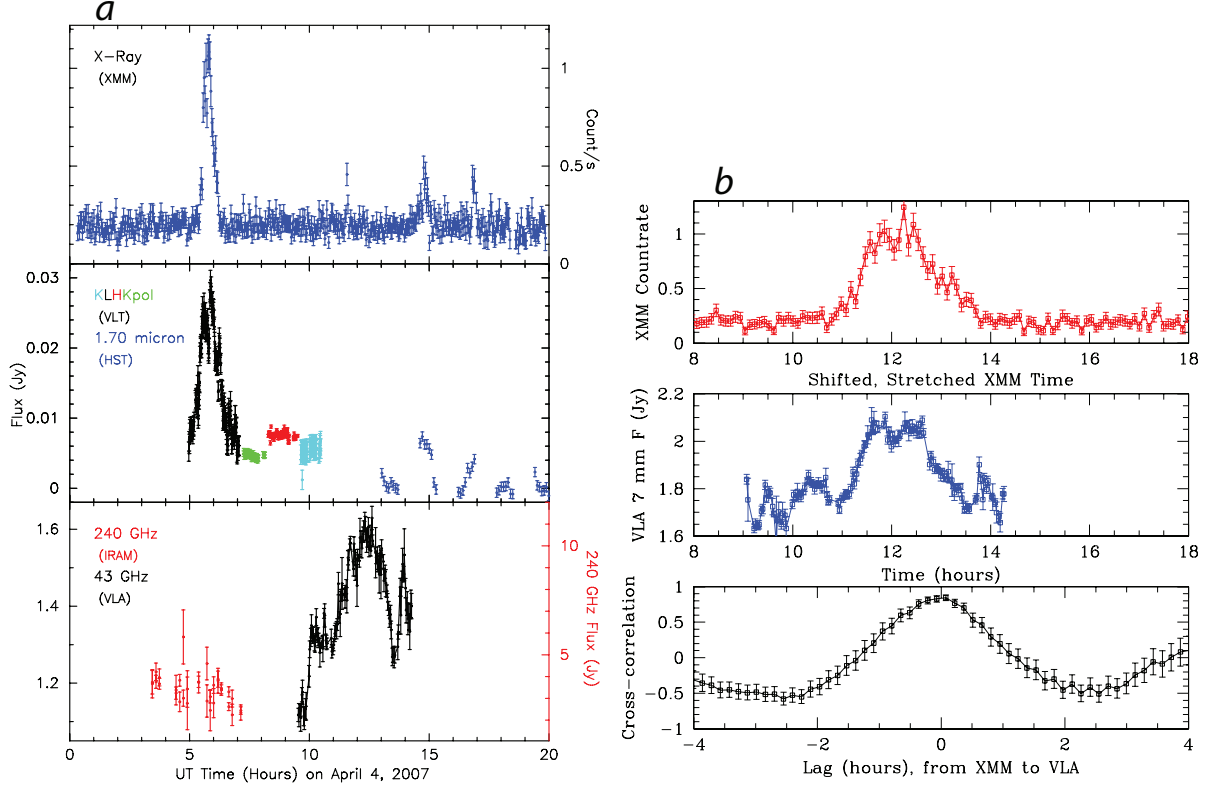


Fig. 24.—: (a - Left) The light curves of Sgr A* on 2007, April 4 obtained with XMM in X-rays (top), VLT and HST in NIR (middle) and IRAM-30m and VLA at 240 GHz and 43 GHz, respectively (bottom). The NIR light curves in the middle panel are represented as H ($1.66 \mu\text{m}$) in red, K_s and K_s -polarization mode ($2.12 \mu\text{m}$) in green and light blue, respectively, L' ($3.8 \mu\text{m}$) in black (Dodds-Eden et al. 2009), and NICMOS of HST in blue at $1.70 \mu\text{m}$. In the bottom panel, red and black colors represent the 240 and 43 GHz light curves, respectively. (b - Right) The top panel shows the light curve of Sgr A* obtained with the XMM, the middle panel shows the light curve taken with the VLA at 43 GHz. The X-ray light curve is shifted by 5.25 hours and stretched by a factor of 3.5. The 43 GHz light curve is baseline subtracted in order to remove the slope due to the quiescent component of Sgr A*. The bottom panel shows the cross correlation plot of the shifted and stretched X-ray light curve with the radio data showing the maximum likelihood delay of 4.6 (-7.6, +9.4) minutes.

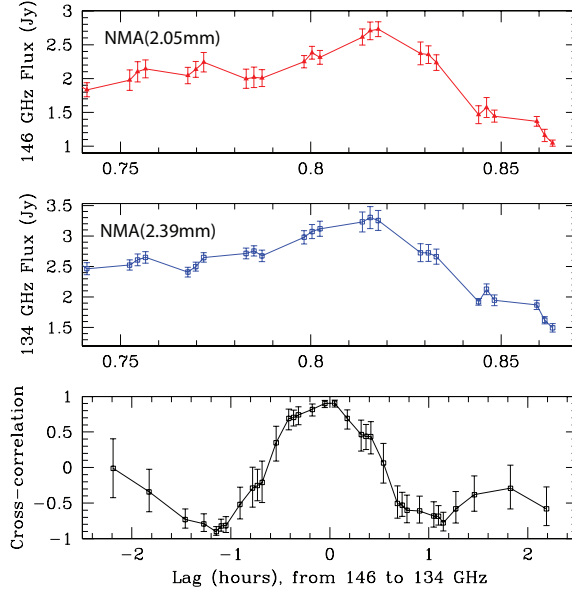


Fig. 25.— The light curves shown in the top and center panels are measured simultaneously with the NMA at 146 GHz and 134 GHz on 2007, April 4, respectively. The cross correlation plot shows a peak with $3_{-8.0}^{+3.4}$ minutes time delay. The time delays in both plots are consistent with zero.

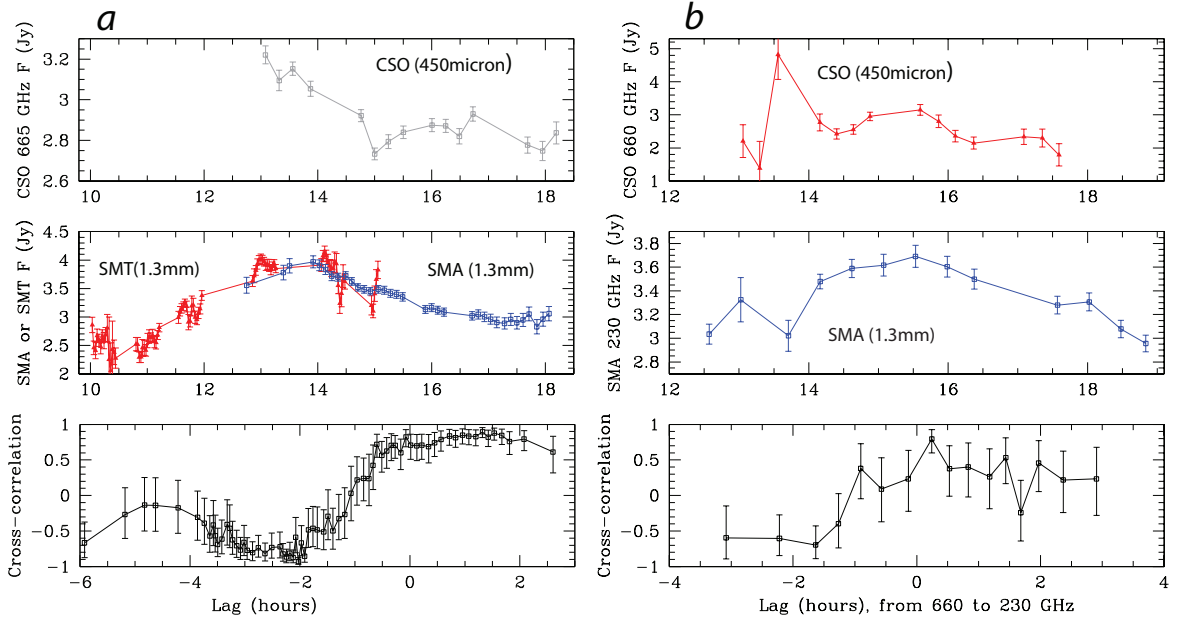


Fig. 26.— (a - Left) The light curve of Sgr A* at $450\mu\text{m}$ (665 GHz) is shown in the top panel whereas the 230 GHz (1.3mm) light curve in the middle panel is based on combining SMT and SMA observations on 2007, April 3 with UT ranges 10:07h - 14:56h and 12:44h - 18:3.8h. A constant offset due to the contamination of a steady background emission is subtracted from the SMT data. The bottom panel represents the cross correlation plot showing a peak with $1.32_{-0.63}^{+0.33}$ hours time delay. (b - Right) Similar to (a) except that the light curves are taken on 2007, April 1 at $450\mu\text{m}$ and 230 GHz using the CSO and SMA, respectively. The peak of the cross correlation shows a $0.24_{-0.29}^{+1.12}$ hours time delay. One σ error bars are given for all the time lags.

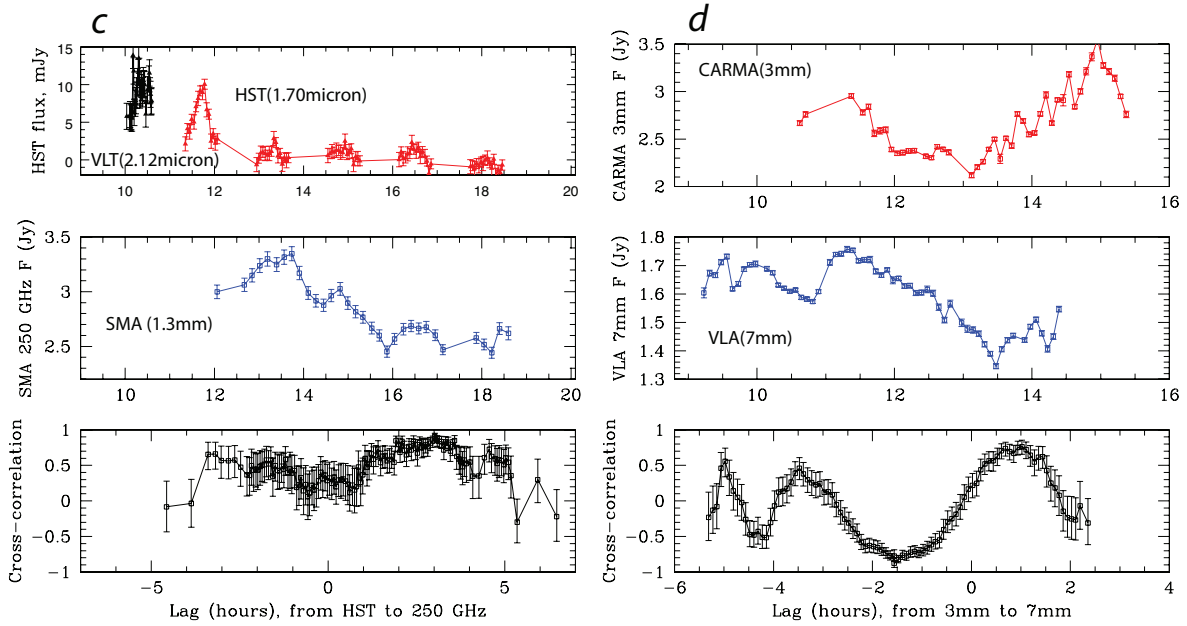


Fig. 26.—: (*c - Left*) Similar to (a) except that NIR light curve is based on combining the data taken with the VLT and NICMOS whereas the 230 GHz data taken with the SMA on 2007, April 5. The cross correlation is constrained to have a peak of $2.64^{+0.5}_{-0.67}$ hours time delay. (*d - Right*) The light curves shown in the top and center panels are based on CARMA and VLA observations at 94 GHz and 43 GHz on 2007, April 2, respectively. The cross correlation plot shows a peak with $1.02^{+0.16}_{-0.31}$ hours of time delay. One σ error bars are given for all the time lags.

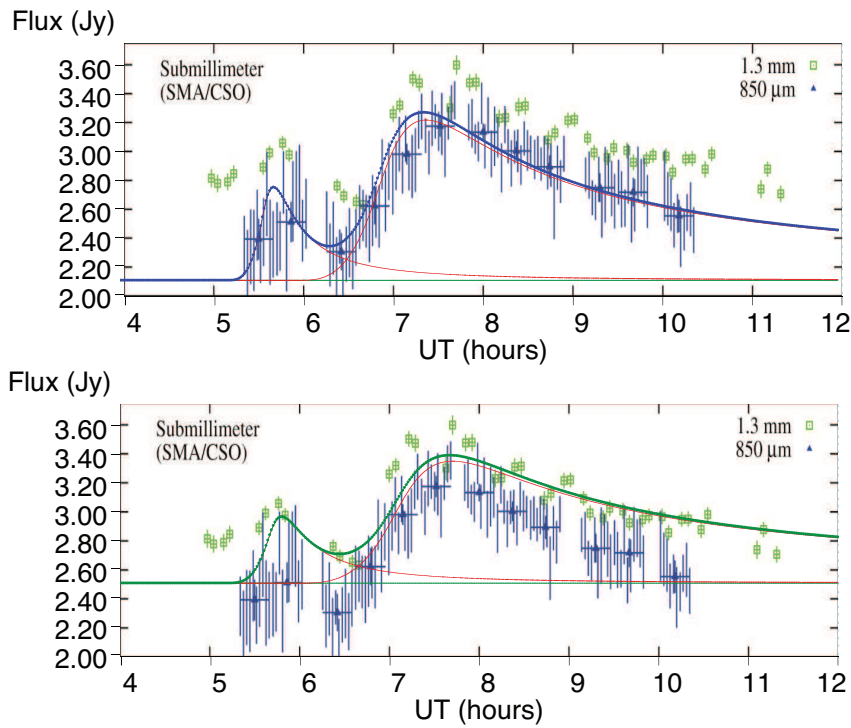


Fig. 27.—: The SMA and CSO data are taken on 2006 July 17 at 1.3mm and 850 μ m, respectively (Marrone et al. 2008). After background subtraction, the two weak and strong flares are fitted simultaneously, supporting the plasmon model. The expanding blob model automatically generates the fit to the 850 μ m data (top panel) in blue and to the 1.3mm data (bottom panel) in green.

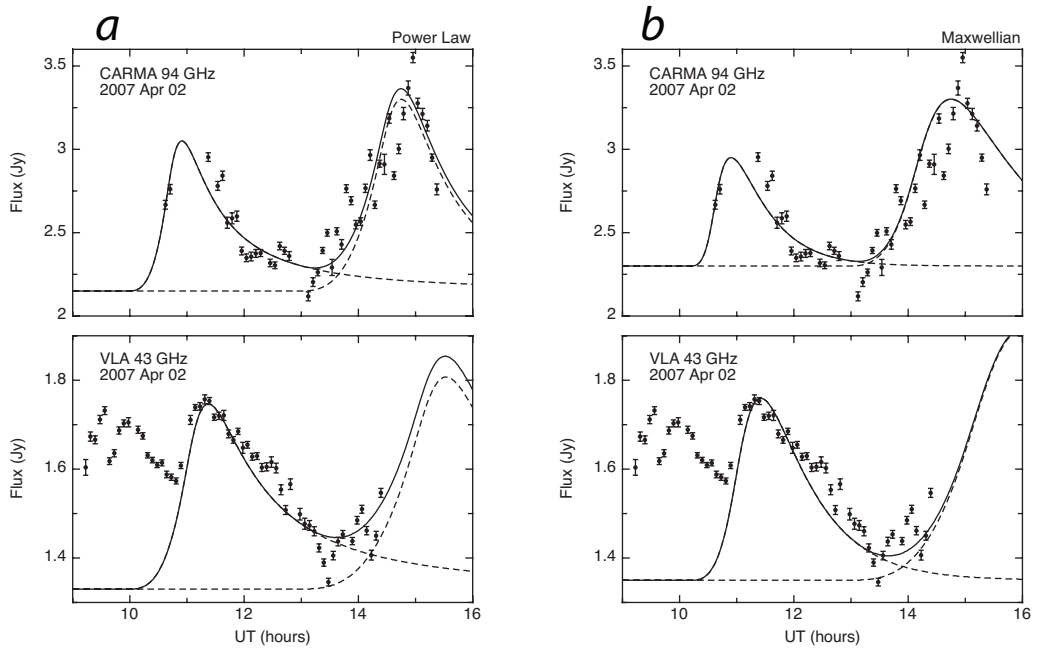


Fig. 28.—: (*a - Left*) A fit to the CARMA data at 94 GHz using two flares are shown in the top panel. The expanding blob model automatically generates the fit to the VLA data at 43 GHz, as shown in the bottom panel. The model has used a power law distribution of electrons. (*b - Right*) Similar to (a) except that a Maxwellian distribution of particles is used to fit simultaneously the CARMA and VLA light curves obtained on 2007 April 2.

